Aerodynamic effects of propulsion integration for high bypass ratio engines

Tomasz P. Stankowski[1], David G. MacManus[2] and Matthew Robinson[3]
Cranfield University, Cranfield, United Kingdom, MK43 0AL

Christopher T. Sheaf [4]
Rolls Royce plc., Derby, United Kingdom, DE24 8BJ

This work describes the assessment of the effect of engine installation parameters such as engine position, size and power setting on the performance of a typical 300 seater aircraft at cruise condition. Two engines with very-high by-pass ratio and with different fan diameters and specific thrusts are initially simulated in isolation to determine the thrust and drag forces for an isolated configuration. The two engines are then assessed in an engine-airframe configuration to determine the sensitivity of the overall installation penalty to the vertical and axial engine location. The breakdown of the interference force is investigated to determine the aerodynamic origins of beneficial or penalising forces. To complete the cruise study a range of engine power settings were considered to determine the installation penalty at different phases of cruise. This work concludes with the preliminary assessment of cruise fuel burn for two engines. For the baseline engine, across the range of installed positions the resultant thrust requirement varied by 1.7% of standard net thrust. The larger engine was less sensitive with a variation of 1.3%. For an assessment over a 10000km cruise flight the overall effect of the lower specific thrust engine showed that the cycle benefits of –5.8% in specific fuel consumption was supplemented by a relatively beneficial aerodynamic installation effect but offset by the additional weight to give a -4.8% fuel burn reduction.

---

[1] PhD Student Researcher, Propulsion Engineering Centre, Cranfield University, United Kingdom
[2] Head of Gas Turbine Technology Group, Propulsion Engineering Centre, Cranfield University, United Kingdom
[3] PhD Student Researcher, Propulsion Engineering Centre, Cranfield University, United Kingdom
[4] Installations Aerodynamics specialist

Nomenclature

A_{ref}	=	wing reference area
b	=	wing span
c_{ref}	=	aircraft reference chord
dc	=	aircraft drag counts, based on aircraft reference area; 1dc = 0.0001
dx	=	horizontal position of the fan cowl trailing edge from the wing leading edge
dz	=	vertical position of the fan cowl trailing edge from the wing leading edge
C_D	=	drag coefficient based on aircraft reference chord
C_f	=	skin friction coefficient
C_p	=	pressure coefficient
C_d	=	discharge coefficient
C_L	=	lift coefficient
C_V	=	thrust coefficient
$C_{Z'}$	=	overall vertical force coefficient including the vertical component of thrust
D_{FF}	=	fan face diameter
D_{max}	=	nacelle maximum diameter
L_{nac}	=	nacelle length
M	=	Mach number
V	=	Velocity
x, y, z	=	Cartesian coordinate system for the aircraft
ξ, η, ζ	=	Cartesian coordinate system for the engine
ξ, R, Θ	=	Cylindrical coordinate system for the engine
ϕ	=	force in the drag domain
θ	=	force in the thrust domain

Acronyms

BPR	=	By-pass Ratio
BPD	=	By-pass Duct
DPW	=	Drag Prediction Workshop

CNPR	=	Core Nozzle Pressure Ratio
CRM	=	NASA Common Research Model
CST	=	Class Shape Transformation function
LPT	=	Low Pressure Turbine
MFCR	=	Mass Flow Capture Ratio
NPF	=	Net Propulsive Force
OPR	=	Overall Pressure Ratio
Soc, EoC	=	Start of Cruise, End of Cruise

I. Introduction

Driven by the requirement of greater propulsive efficiency for turbofan engines, there has been a trend to increase the engine by-pass ratio [1]. To achieve the expected improvement in the overall aircraft efficiency, it is necessary to ensure that the installation and integration of the engine with the airframe is understood. Currently, the overall effect of engine installation for a typical conventional podded under-wing engine on a wide-body twin-engine aircraft is estimated to be in the order of 30 to 50 drag counts per two engines [2], which corresponds to approximately 10% to 15% of aircraft total drag. This penalty is sensitive to the relative engine size and position on the wing [2, 3, 4] and the effect of engine size becomes significant for larger diameter engines [5]. The presence of a relatively larger engine can result in a flow acceleration on the lower side of the wing and eventually in the loss of lift [5]. This local acceleration of the flow due to the larger nacelle and pylon can also lead to penalising interference effects [6]. However, some efforts can be undertaken to redesign the wing specifically for the larger engines to mitigate the loss of lift [7]. Furthermore a careful redesign of the pylon [8] to move the peak acceleration downstream can lead to a drag reduction of 6dc. Due to the large number of degrees of freedom, computational methods such as full potential flow [9] or Euler [10] evaluations have been considered to analyse the multitude of possible configurations [9, 10]. Furthermore, the development of numerical tools and an increase in computational power led to a series of AIAA Drag Prediction Workshops, where the second workshop was dedicated to propulsion installation effects [11]. The outcomes from the 2nd DPW [11] triggered the design of more a modern aircraft geometry for the NASA Common Research Model (CRM) [12]. The publication of substantial experimental datasets with and without through-flow nacelles [13, 14] makes CRM a benchmark validation activity to assess the effects of

installation. Subsequent to the work undertaken here, the effects of installation of a through-flow nacelle on the CRM were addressed during the 6th Drag Prediction Workshop [15]. Initial results from the CRM workshop show that the installation drag of a through-flow nacelle is approximately 23 dc based on both the experiment as well as the RANS CFD calculations using multi-block structured meshes. The installation drag of 23 dc corresponds to approximately 10% of total aircraft drag. Within this broad context, it is anticipated that engine installation will become an increasingly important issue as engine diameters are expected to increase relative to the size of the aircraft. It is also expected that knowledge of these aspects at the preliminary design stage will become more important to facilitate timely and informed decisions on engine cycle, size and airframe integration. The aim of this research is to study the details of aerodynamics for aero-engine installation at cruise condition for a typical 300 seater aircraft. The work was carried out with use of the NASA CRM which was modified to include an under-wing turbofan engine with a separate-jet exhaust system. The paper concentrates on the effect of engine position, size and power setting on the overall installation effect for a re-trimmed aircraft. All the presented computational results come from the Reynolds Averaged Navier-Stokes studies. The comparison of the computations for the full aircraft configuration with those for the combined results for the isolated engine and clean-wing airframe enable the interference effects [16] to be determined.

II. Methods and scope

The main focus of the work is to evaluate installation aerodynamic effects for podded underwing engine configurations by the means of computational fluid dynamics (CFD), in particular the computation of Reynolds Averaged Navier-Stokes (RANS) equations with the commercial solver ANSYS Fluent. This solver was previously used for the calculation of the CRM aerodynamic characteristics and the effect of the TFN [17] as well as for the assessment of dual stream exhaust system performance [18]. The assessment of the overall installation effects at cruise condition for a relatively modern aircraft configuration [12] is performed. The ambition is to provide detailed analysis of the individual effects, evaluate the overall installation effect due to the aerodynamics and to compute the cruise fuel burn for the combined aircraft-engine system.

A. Project scope

The overall project scope is to assess the impact of engine installation at cruise conditions as it is the dominant phase for long-haul flights. A typical mission at an altitude of 35000 ft and a cruise Mach number of 0.82 was chosen

within a range of aircraft angles of attack from 0°and 5°. For a given mission specification, the NASA CRM [12] was chosen, which is comparable with a typical twin-engine wide-body 250-300 seater aircraft. A range of engine positions was considered based on the location of the fan cowl trailing edge in relation to wing leading edge (Fig. 1, Fig. 2). The aim within this work is to evaluate the characteristics over a relatively wide range of engine positions (Fig. 2). However, within this context, this range of positions also encompasses previously reported [19] approximate locations for conventional installations on the Boeing B757, B767 and B777 which are generally in the region between points C1 and C2 (Fig. 2). Moreover, the sensitivity of engine installation effect to engine size is considered. Furthermore, to enable the assessment of the engine installation, a clean wing aircraft, as well as isolated engine configurations are computed. It is necessary to compare the combined engine-airframe configuration, a clean-wing aircraft and an isolated engine to fully evaluate the installation effects.
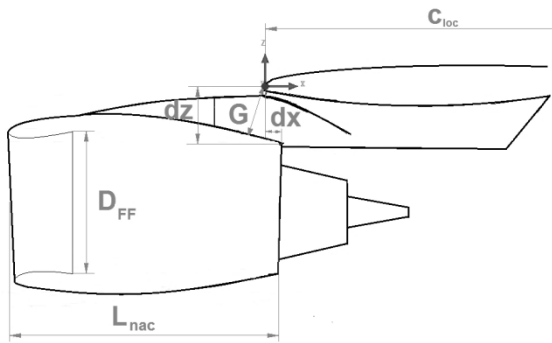
Fig. 1 Sketch of key installation parameters
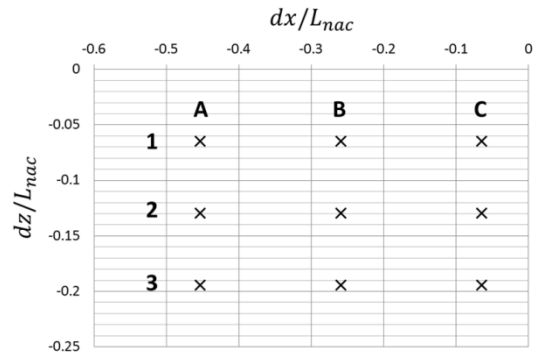
Fig. 2 Map of investigated engine positions for baseline engine

B. Engine model

To provide a range of realistic CFD boundary conditions for an engine, a full engine performance model was developed for a required specification. The engine performance modelling was done with use of the Cranfield University in-house code, Turbomatch [20]. Turbomatch is a zero- dimensional code for aerothermal analysis that employs discrete component maps. The method solves for the mass and energy balance between the various engine components. Within the current scope of work, the engine is assumed to be operating exclusively under steady-state conditions.

Based on the CRM performance at $M = 0.82$, a net thrust requirement of 55686 N at an altitude of 35000 ft. was estimated. An engine performance model for a typical modern turbofan-engine (BPR=10.4, OPR=50) has been created to match the specification, and is referred to as the baseline engine (E1). Decisions on engine technology level were taken based on open source data [1] for engines of comparable thrust class. Furthermore, an engine performance model with a very-high by-pass ratio (BPR=17.8, OPR=58) for the same mission specification was created. While the engine by-pass ratio increased, the engine architecture, thrust requirement and component technology level were kept constant. The engine performance models were used to generate engine boundary conditions to provide a consistent link between the engine intake and the engine nozzles. Based on the engine performance model, the baseline engine (E1) the start of cruise 'SoC' setting (Table 1) is characterized by the massflow capture ratio (MFCR) for the cruise condition of 0.75, the fan nozzle pressure ratio (FNPR) of 2.71 and the core nozzle pressure ratio (CNPR) of 1.37. Similarly for the study of engine size, the larger engine (E2) 'SoC' power setting is represented by MFCR of 0.75, FNPR of 2.11 and CNPR of 1.68. With use of performance models, the range of power settings from start of cruise to start of descent was considered.

Table 1 The range of power settings for engine E1

| Power Setting	E1			E2		
	MFCR [-]	FNPR [-]	CNPR [-]	MFCR [-]	FNPR [-]	CNPR [-]
PS1 'SoC'	0.75	2.71	1.37	0.75	2.11	1.68
PS2	0.7	2.51	1.27	0.7	1.98	1.44
PS3	0.65	2.32	1.20	0.65	1.83	1.25
PS4	0.6	2.12	1.14	0.6	1.70	1.11

Based on the performance model of the baseline engine with a reference fan face diameter ($D_{FF\ Base}$), an axisymmetric geometry of an engine nacelle was created (Fig.3). An established methodology [21, 22, 23, 24] was used to determine the engine keypoints such as fan hub, fan tip, intake throat, intake highlight, nacelle maximum

diameter, nacelle trailing edge, and key dimensions of the exhaust ducts. The geometry was constructed using class shape transformation (CST) curves [21, 22, 23, 24, 25, 26] to provide a smooth curvature distribution. The increase of by-pass ratio for engine E2 resulted in an increase of fan diameter of $1.23D_{FF\ Base}$. The same conventional preliminary design guidelines and the same methodology as for the baseline engine E1 were implemented. As a result a geometrically similar nacelle for the E2 engine was created. As the design was performed for a different engine BPR, the exhaust system was sized appropriately. To maintain the similarity of the design, the same boat-tail angles for the core cowl and plug as for the baseline engine were used.

C. Computational method

The aerodynamic analyses were performed using a compressible RANS method. An implicit flow solver was used with second order discretization for all terms. The Green-Gauss node based gradient method was used and, based on the results from 4th AIAA Drag Prediction Workshop (DPW) [27, 28], the $k - \omega\ SST$ turbulence model was used [29]. The aircraft with an installed engine was placed in the computational domain with a size of $100c_{ref}$ (Fig. 4) which was adopted based on the conclusions from the 4th DPW [28]. A pressure far-field boundary condition was used by specification of freestream Mach number of M=0.82 and static pressure and static temperature based on International Standard Atmosphere (ISA) for 35000 ft. A centreline symmetry boundary condition was used as half of the aircraft model was computed. The studies of the isolated engine are considered. The Dual Stream Flow Reference Nozzle (DSFRN) [18,30] was identified as suitable test case for the validation of numerical method in the determination of thrust for separate-jet exhaust systems. The numerical strategy coherent with current research was followed for the computations [31] of the DSFRN [18] with use of $k - \omega\ SST$ turbulence model [29] and full resolution of the boundary layer with $y^+ = 1$. The by-pass duct entry and low pressure turbine exit were set to be uniform total pressure inlets. All the nozzle and by-pass duct walls were modelled as no-slip, adiabatic boundary condition. Within the current work, the isolated engines with an intake geometry were computed to compare with the wing-installed engines. The engine fan face was set to pressure outlet with a target mass-flow and pressure inlets were used for the by-pass duct (BPD) entry and low pressure turbine (LPT) exit. All the nozzle and by-pass duct walls were modelled as no-slip, adiabatic boundary condition. In the computations the iterative convergence was monitored for the forces that act on the geometry. The amplitude of the oscillation found in the

forces report did not exceed an equivalent of 0.2 aircraft drag counts for all the computations, which is 0.1% of total aircraft drag.
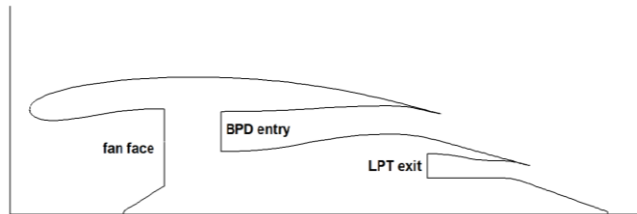
Fig.3 Schematic of the baseline engine (E1).
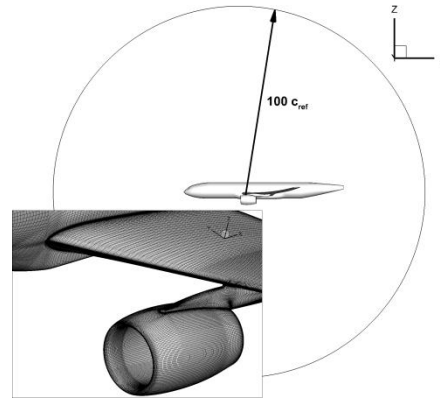
Fig. 4 The hemispherical domain for aircraft studies and close-up on the mesh.

D. Gridding methods

For the reference "clean" aircraft studies, the grid independence assessment followed the approach advocated by Roche [32]. Based on the gridding guidelines [27], a medium density structured mesh was created ("WBT0 medium") with an element count of around 10×10^6 elements. Four meshes were generated for the clean wing aircraft (WBT0) and the impact of spatial resolution on aircraft drag $C_{D\,A/C}$ was evaluated under typical cruise conditions ($M = 0.85$ and $AoA = 2.5°$). The refinement ratio between the meshes was 1.15 in each direction. The boundary layer mesh was kept unmodified to have the same node distribution and the first cell height resulted in $y^+ = 1$ for all mesh densities. As a result, the meshes of 6.9×10^6, 10.3×10^6, 16.1×10^6, and 24.1×10^6 cells were created and referred to as "coarse", "medium", "fine" and "superfine" respectively. Richardson Extrapolation [32] was conducted to estimate the grid independent solution. The aircraft drag coefficient $C_{D\,A/C}$ reduced monotonically with increasing mesh size. Using a factor of safety of 1.25, the second order grid convergence index (GCI) for a medium mesh solution was 2.05% and 1.08% for fine mesh solution. The refinement ratio was in each case evaluated as an average based on the three meshes. Following Roache [32], the achievement of the asymptotic range can be checked by a simple ratio of GCI corrected with use of the refinement ratio between the meshes and the observed order of computation. A satisfactory result was achieved for the GCI of medium-fine and fine-superfine with a ratio of 1.018. Thus, the fine meshes were used in the paper.

For the meshes with through flow nacelles (TFN), a structured mesh with a comparable blocking strategy to the clean wing configuration was created. Additional blocking was created to accommodate the presence of through flow nacelles. The blocking around the nacelle is arranged as an O-grid concentric with the engine axis. The meshing of the TFN geometry was based on the experience from previous studies on isolated studies [17, 33, 34]. Thus, the following criteria were added: 40 elements for the nacelle lip, maximum axial spacing on the nacelle $\Delta x = L_{nac}/110$. Those criteria have been merged with most of the DPW4 gridding guidelines [27]. The guidelines for trailing edges as well as for longitudinal and lateral spacings were consistent with DPW4 gridding guidelines [27]. However, the near wall treatment was facilitated with a constant $y^+ = 1$ for all mesh resolutions and with minimum 20 nodes within boundary layer. In total, three mesh densities were used for the aircraft with a through flow nacelle and the overall number of elements in the meshes are 16×10^6, 22×10^6 and 30×10^6. The meshes are called "coarse", "medium" and "fine", respectively. Also the meshes are the derivations from the clean wing meshes and the applied modifications are localized around the through-flow nacelles. Similarly, the Richardson Extrapolation [32] was then conducted to estimate the grid independent solution for cruise condition ($M = 0.83$ and $AoA = 2.5°$). The aircraft drag coefficient $C_{D\ A/C}$ reduced monotonically with increasing mesh size. Using a factor of safety of 1.25, the second order grid convergence index (GCI) was 1.2% and 0.5%.

As part of the work to enable an analysis of the installation effects, the isolated engines were considered with the separate jets exhaust. The Dual Stream Flow Reference Nozzle (DSFRN) [18,30] was chosen as a validation test case for the computation of the separate jet nozzles. The computations were done [31] with structured meshes with $y^+ = 1$ for full boundary layer resolution. The domain study was completed [31] at a FNPR of 2.2 for three domain diameters, $20D_{max}$, $40D_{max}$ and $60D_{max}$ where D_{max} was the maximum diameter on the DSFRN nacelle. Between the $20D_{max}$ and $60D_{max}$ computations there was an increase of 0.5% in the overall C_V, 0.003% in C_D^{BPD} and a decrease of 0.12% in C_D^{Core}. The $60D_{max}$ was adopted for further study on the DSFRN. To determine the grid dependency, a total of three mesh resolutions were investigated at a FNPR of 2.2 such that grid independency could be assessed with Richardson Extrapolation [32] used to calculate the grid independent solution. The first cell height remained fixed across all the meshes investigated. The element count for the three meshes was as follows: 8.6×10^6, 10.3×10^6, 14.5×10^6. A monotonic increase of thrust coefficient was observed with the mesh refinement, with a GCI

0.06% between the 8.6 x10^6 element and 10.3 x10^6 element meshes and the GCI of 0.08% between the 10.3 x10^6 element and the 14.5 x10^6 element meshes. A safety factor of 1.25 was used throughout. The results presented in this paper were computed on the 14.5 million element mesh .

The separate jet engine geometry is of key interest in the current research both in terms of the isolated engine as well as for the installed configurations. The intake and nacelle meshing strategy was similar to that adopted for the TFN 'fine mesh'. The nacelle meshing guidelines were established based on previous studies [35]. However, the bypass duct, core duct, nozzles and core cowl required a modified blocking strategy which also facilitated the boundary layer meshes. A blocking topology compatible with DSFRN was developed. Three mesh resolutions for the isolated engine were created with 3.0x10^6, 9.8x10^6, 33.5x10^6 elements and with use of the Richardson Extrapolation [32] the grid dependency study was done. For the isolated engine at an equivalent cruise incidence of 4.25°, the engine net propulsive force NPF reduced monotonically with increasing mesh size. Using a factor of safety of 1.25, the second order grid convergence index (GCI) was 1.5% from coarse to medium mesh and 0.64% from medium to fine. The GCI was also computed for the engine thrust coefficient with 0.007% and 0.002%. The effect of the computational domain was also assessed and for the separate-jet configuration indicated an increase of the engine net propulsive force with an increase of domain diameter by +0.07% from 10 to 30D_{max} and an reduction of Net Propulsive Force (NPF) by -0.11% from 30 to 50D_{max}. The non-monotonic behaviour is explained by a pressure influence from the pressure far-field for the 10D_{max} domain. For this work the extent of the domain size was set to 50 nacelle D_{max}. As a result a mesh with 9.8 x10^6 elements was used for the isolated engines (E1 and E2) with separate exhausts and the meshing strategy is consistent with the 'fine' mesh resolution in the aircraft studies.

For the full engine geometries positioned under the wing, the meshing strategy was similar to that adopted for the TFN under the wing. As for the isolated separate jet configuration, the mesh had to facilitate the boundary layer meshes for the bypass duct, core duct, nozzles and core cowl. The inclusion of the separate jet meshing rules resulted in the nominal mesh of 35 x10^6 elements for the configuration of CRM with the engines installed. The mesh was derived from the fine mesh for the clean wing configuration.

E. Drag accounting methods

In the current work, a thrust and drag book-keeping system based on AGARD book-keeping system was followed [17, 34, 36, 37]. As a result, a modified near-field method of drag computation for separate jet engines is used. The domain is split into a drag domain and thrust domain. The forces that act in the thrust domain (Fig. 5), i.e. on the inside of the streamtube, are denoted as θ and the forces in the drag domain are denoted as ϕ. Furthermore, gauge stream forces of the flow are evaluated at characteristic engine stations from upstream to downstream infinity and are denoted F_{G0} and F_{G00} , respectively.
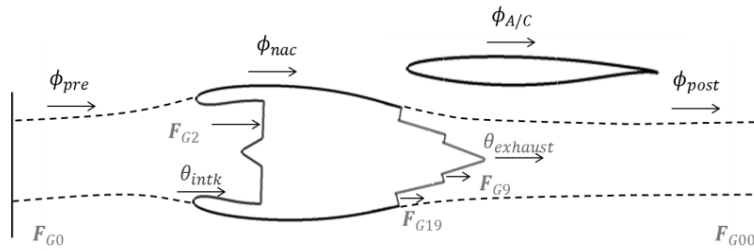
Fig. 5 Decomposition of modified Near Field Method forces acting on the entry streamtube and nacelle

To account for all the forces of an isolated or wing-installed engine, the NPF is considered as the difference of the overall engine thrust (F_{ov}) and nacelle drag (D_{nac}) in the drag aero-axis (Equation (1)). From the balance of forces for the post-exit domain, the unknown terms F_{G00} and ϕ_{post} from Equation (1) can be substituted by the known terms of stream forces (F_{G9} and F_{G19}) and forces that act on the exhaust surfaces ($\theta_{exhaust}$). As a result, the NPF can be expressed in terms of standard net thrust (F_N) and forces exerted on exhaust surfaces ($\theta_{exhaust}$), forces on the nacelle (ϕ_{nac}) and the force on the pre-entry streamtube (ϕ_{pre}) (Equation (2)). By the introduction of modified standard net thrust (F^*_N) and modified standard drag for the nacelle (D^*_{nac}) (Equations (3) (4)), the NPF can be expressed in terms of F^*_N and D^*_{nac} alone (Equation (5)). To compute the balance of forces in the drag aero-axis for an engine and an aircraft an overall horizontal force ($F_{x'inst}$) is considered as the difference between NPF and airframe drag ($D_{A/F}$). To determine the magnitude of the interference forces the configuration needs to be compared with the idealised configuration with the idealised configuration with no interference force. Following the established approach to determine interference terms [16], a superposition model (SM) of the clean-wing and isolated engine is created. Within this SM estimate, the values of lift and drag of the clean-wing aircraft are

combined with the isolated engine thrust, drag and lift data at the corresponding incidence. As a result the overall horizontal force of the superposition model is obtained ($F_{x'SM}$). Clearly this model does not take into account any of the mutual interference terms that arise between the engine and airframe and which affect both the lift and drag terms. The sole purpose of the superposition model is to provide a reference for the engine-airframe configuration. Eventually, the aerodynamic interference term F_{interf} is the difference between RANS computations for the combined engine-airframe configuration and the idealised SM at equal overall lift force (Equation (7)). The overall aerodynamic interference consists of the individual effects of installation on the drag and thrust terms. The individual effects are referred to as the airframe interference drag (Equation (8)), the engine interference drag (Equation (9)) and the interference thrust (Equation (10)). To obtain the force coefficients based on the aerodynamic forces, the freestream reference condition is used, where ρ is the mass density of the fluid, υ is the velocity of the fluid and A_{ref} is the aircraft reference area. As a result, the nacelle drag coefficient (C_{D^*nac}) is defined (Equation (11)) based on the nacelle drag and the aircraft total drag coefficient (Equation (12)) is defined based on the sum of the drag forces for the nacelle and the airframe.

$$NPF = F_{ov} - D_{nac} = F_{G00} - F_{G0} - \phi_{pre} - \phi_{nac} - \phi_{post} \tag{1}$$

$$NPF = F_N - \theta_{exhaust} - \phi_{pre} - \phi_{nac} \tag{2}$$

$$D^*{}_{nac} = \phi_{pre} + \phi_{nac} \tag{3}$$

$$F^*{}_N = F_N - \theta_{exhaust} \tag{4}$$

$$NPF = F^*{}_N - D^*{}_{nac} \tag{5}$$

$$F_{x'} = NPF - D_{A/C} = F^*{}_N - D^*{}_{nac} - D_{A/F} \tag{6}$$

$$F_{interf} = F_{x'inst.} - F_{x'SM} = \Delta F^*{}_N - \Delta D_{A/F} - \Delta D^*{}_{nac} \tag{7}$$

$$\Delta D_{A/F} = D_{A/F\ installled} - D_{A/F\ clean-wing} \tag{8}$$

$$\Delta D^*{}_{nac} = D^*{}_{nac\ installed} - D^*{}_{nac\ isolated} \tag{9}$$

$$\Delta F^*{}_N = F^*{}_{N\ installed} - F^*{}_{N\ isolated} \tag{10}$$

$$C_{D^*\ nac} = \frac{D^*{}_{nac}}{\frac{1}{2}\rho\upsilon^2 A_{ref}} \tag{11}$$

$$C_{D\ tot} = C_{D\ A/F} + C_{D^*\ nac} \tag{12}$$

F. Aircraft performance and fuel burn calculation

In addition to the assessment of the effect of engine installation on the elements of interference and the overall changes in lift and drag, it is of interest to undertake a preliminary evaluation of the impact on fuel burn. Within the current work a typical preliminary design approach of fuel burn analysis at the cruise phase is considered. A point mass model of the aircraft is considered at the constant altitude and the constant flight Mach number. The balance of forces on the aircraft needs to be obtained to result in steady state flight as a basis of the calculations. The initial mass of the aircraft at the start of the cruise phase is determined based on the BADA methodology [38] for a typical 250-seater aircraft. As a preliminary assessment, the climb phase was modelled [38] as independent of the type of engine used for the cruise calculation. As a result, the fuel burnt during the climb phase was deducted from the maximum take-off mass of the airplane and the aircraft mass at start of cruise for baseline configuration was established. The mass of the propulsion system is included in the overall aircraft mass for the baseline configuration (E1). To determine the additional weight for larger engine (E2), the mass of the propulsion systems was estimated based on the statistical correlations for engine mass [39] and nacelle mass [40]. The bare engine mass is estimated based on the WATE++ method [39]. The method is a statistical approach to engine weight estimation based on the overall pressure ratio, by-pass ratio and core massflow. This method has been calibrated based on a range of engines with a reported uncertainty [39] of $\pm 10\%$ on the mass estimation for engines ranging in thrust from 120 to 400 kN. The WATE++ tool was assessed against known engines of a similar class (BPR, OPR, thrust) to the E1 engine and a discrepancy of -3% on engine mass was noted which is considered to be satisfactory within the performance of statistical methods [41]. The nacelle mass estimation is based on Jenkinson et.al [40]. This uses a piecewise linear model based on the take-off thrust of the engine. The weight of thrust reversers was taken into account while establishing the method. Based on previous studies [33], the uncertainty of the method was found to be $\pm 10\%$. Moreover, the nacelle mass was estimated for the E1 and E2 engines and it equates to 25% of the total engine mass which is in agreement with current reported technology levels [42]. From the quadrature method for the assessment of uncertainties [43] the overall combined uncertainty on the propulsion system mass is $\pm 3.4\%$. Based on the mass estimation for the entire propulsion system, the weight penalty for the larger engine E2 is evaluated and added to the mass of the baseline aircraft configuration at the start of cruise ('SoC'). With use of the aircraft mass for 'SoC' the weight and therefore the lift requirement of the aircraft is established. For each configuration, the overall lift including the vertical component of thrust is considered. Based on the required lift, the corresponding drag value is

evaluated based on the CFD computed drag polars for the considered configurations with additional corrections for parasitic drag. Furthermore, the thrust requirement is set based on the drag of the aircraft. However, the drag of the configuration contains the thrust dependent terms and therefore it is an iterative process to balance the thrust and drag at a given lift coefficient. Once the balance of forces on the aircraft is achieved the first step of the cruise computation is computed and the fuel burn is evaluated. The mass of fuel burnt at that step is subtracted from the 'SoC' aircraft mass and the procedure is repeated for the next step. To provide relatively small steps for the integration process, the cruise phase was divided in to 40 steps to consider steps shorter than 20 minutes [44] of steady flight.

III.   Results

A. Validation

The validation of the CFD method addresses two parts that are the building blocks of the current research. The first part assesses the capability of CFD to determine the installation drag. The NASA CRM was used as a representative modern aircraft with its wing designed [12] for M=0.85 and C_L of 0.5. The aerodynamics for the CRM with Through Flow Nacelles (TFN) were experimentally investigated [13, 14] using a 1/37th sub-scale model at a Reynolds number of 5x10^{6}. The second part of the validation work is concentrated on the validation of the jet exhaust flow with use of the AIAA Dual-Flow Reference Nozzle (DFRN) test case [18, 30]. The assessment of CFD for the exhaust flow is based on the comparison of current computations [31] with the experimental results [18] for the DSFRN.

1. Aircraft validation with and without through flow nacelle

The validation activity for the clean aircraft [17] investigated the mesh dependence, sensitivity to turbulence models and compared the computed results with the measurements by Rivers [13] , as well as with the computation studies from participants of DPW4 presented and Tinoco [28]. The experimental data by Rivers [13] was corrected for the presence of the wind tunnel walls, but remained uncorrected for the presence of the sting. The results for the fine mesh with the $k - \omega$ SST turbulence model have a $+13dc$ (5% of airframe drag) discrepancy at the cruise condition

of $M = 0.85$ and $C_L = 0.5$. The average of the results from the DPW4 has a $+5.5dc$ difference from the experimental data with a $\pm 10dc$ scatter. Within the current work an evaluation with the $\gamma - \theta$ transition model on the medium mesh provide a +6dc difference between the CFD and measurements at the cruise condition ($M = 0.85$ and $C_L = 0.5$). To expand the validation, analyses for the CRM configuration with and without the nacelle and pylon were computed with three mesh resolutions. To validate the computation for the aircraft at the condition closest to the chosen mission profile for the engine-airframe configurations, the Mach number of 0.83 was chosen from the experimental dataset [13]. The results for the wing body (WB) configuration and the wing body nacelle pylon (WBNP) configuration were compared with the measurements (Fig. 6). With the increase of mesh resolution for the WB configuration the difference between the computed and measured drag at $C_L = 0.5$ reduces monotonically from 16.2 dc to 8.6dc for the coarse ($6.9x10^6$ elements) and fine mesh ($14.7x10^6$ elements) respectively. As for the WBNP configuration, the drag discrepancy reduces from 15.3dc for coarse mesh ($15.7x10^6$ elements) to 10.3dc and 8.4dc for medium ($22.4x10^6$ elements) and fine mesh ($29.7x10^6$ elements), respectively.

The penalty associated with the installation of the TFN in terms of the installation drag ($\Delta C_{D\ inst}$) was determined for the computations for each mesh resolution and compared with the installation drag determined from the experimental drag polars (Fig. 7). The computation broadly captured (Fig. 7) the magnitude of 25dc for installation drag ($\Delta C_{D\ inst}$) and the magnitude was approximately constant across the range of C_L from 0.15 to 0.55. For higher C_L, the $\Delta C_{D\ inst}$ reduces rapidly beyond $C_L = 0.6$ and equals zero at about $C_L = 0.65$. The reduction of $\Delta C_{D\ inst}$ is predominantly the result of an increased contribution of the TFN to the aircraft lift C_L with relatively constant drag contribution to C_D at higher aircraft incidence. The results for all the mesh resolutions are within 3dc for the range of lift coefficient from 0.4 to 0.6. The best accuracy is achieved for the fine mesh resolution with 1dc discrepancy across the range of interest (C_L from 0.4 to 0.6). The behaviour of the installation drag ($\Delta C_{D\ inst}$) was found to be non-monotonic with respect to the mesh resolution. Even though the aircraft drag ($C_{D\ tot}$) was reduced monotonically with the increase of the mesh resolution for both configurations with and without TFN, the rate of the reduction was different for each geometric configuration (Fig. 6). As a result, the $\Delta C_{D\ inst}$ for the "coarse" mesh presented relatively good results as a result of cancellations of mesh dependent terms (Fig. 7). The "fine" mesh solutions were more accurate on both the absolute values of $C_{D\ tot}$, as well as the $\Delta C_{D\ inst}$. Within this work the fine mesh approach, with a 1dc difference in $\Delta C_{D\ inst}$ between the computations and the measurements, has been used for

the subsequently reported results. This finding is in agreement with the initial results from 6th DPW [15], where no improvement in the accuracy for $\Delta C_{D\ inst}$ is reported for structured meshes denser than 20 million elements.
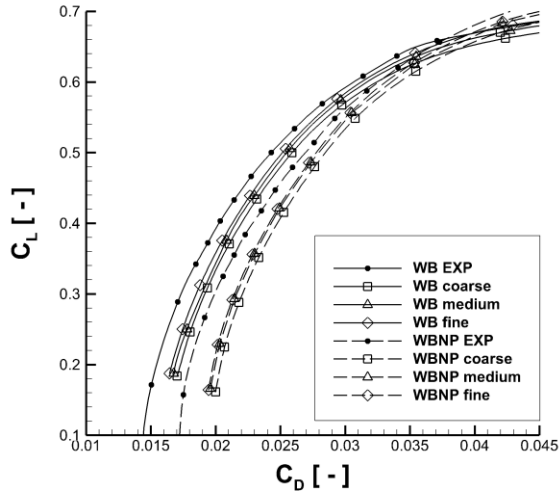
Fig. 6 Drag polar for the CRM without (WB) and with nacelle and pylon (WBNP).
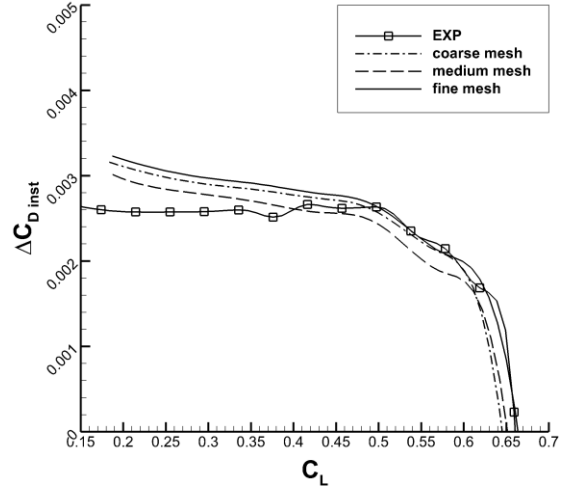
Fig. 7 Installation drag coefficient ($\Delta C_{D\ inst}$) for WBNP against C_L; compared with measurements [13]

2. Dual Flow Reference Nozzle (DFRN)

To validate the numerical methods for the calculations of the nozzle performance metrics for separate-jet exhaust systems study was performed based on the DSFRN configuration [18]. The typical nozzle performance parameters such as overall thrust coefficient (C_V) and discharge coefficients for both core (C_d^{Core}) and by-pass (C_d^{BPD}) nozzles were chosen for the comparison between the simulations and measurements [18]. The effect of domain size, mesh resolution and iterative convergence were assessed as part of the work by Otter [31]. Due to the main interest in the cruise performance of engines within the current study, the fan nozzle pressure ratios (FNPRs) from 2.2 to 2.6 for the DSFRN are the most significant. The discrepancy for overall C_V as compared with experimental data is less than +0.1% for the FNPRs between 2.2 and 2.6. In comparison, the computational results [30] from the AIAA PAW2 workshop had an average difference in computed overall C_V was -0.4% with a scatter of computational data by $\pm 0.5\%$. As for the bypass (C_d^{BPD}) and the core discharge coefficient (C_d^{Core}) the average difference was -0.44% and -0.62% across the cruise range of FNPR. The previous studies [30] have reported average differences in the range of -0.4 and -0.6 %, for bypass and core respectively.

B. Isolated engines

To evaluate the effect of engine size on the isolated engine performance, two engines are considered. A baseline engine (E1) and a larger, low specific thrust engine (E2) with a D_{FF} 1.23 times larger than E1 engine. Both engines are designed to generate the same standard net thrust at cruise condition. Thus, prior to engine installation on the airframe, the computation of the isolated engines (Fig. 8a and b) across a range of incidences from $0°$ to $8°$ was performed at the cruise $M = 0.82$, MFCR=0.75 for both engine. Due to the different thermodynamic cycles (Table 1), the engines operate with FNPR=2.71 and 2.11 as well as CNPR=1.37 and 1.68, for baseline engine E1 and larger engine E2 respectively. The results are presented in aircraft drag counts for the full aircraft geometry and therefore the drag values for two isolated engines are presented.

For the baseline engine E1, the modified nacelle drag coefficient (C_{D^*nac}) for two engines is approximately 35 dc at $AoA_{eng} = 0°$. The drag coefficient for the isolated engines (C_{D^*nac}) was quadratic across the incidence range of incidence from $0°$ to $8°$ with 41dc at $8°$. The cruise condition presents an effective incidence onto the installed engine of approximately $AoA_{eng} = 4.25°$. The AoA_{eng} is a result of summation of the aircraft angle of attack at cruise ($AoA_{A/C} = 2.5°$) with the geometric installation angle for the E1 engine of $AoA_{inst} = 1.75°$. The engine installation angle is considered to be acceptable based on the comparison with the installation angle of $AoA_{inst} = 1.5°$ for the CRM through-flow nacelle. At $AoA_{eng} = 4.25°$, the pair of isolated engines has a C_{D^*nac} of 36dc which is approximately 15.4% of the clean aircraft total drag. Compared with the baseline engines, the larger engines 'E2' (Fig. 8b) has a C_{D^*nac} of 50 dc at $AoA_{eng} = 0°$ with this increase in C_{D^*nac} approximately proportional to the increase in wetted area. Moreover, other secondary effects on the drag value are present such as a modest effect of the Reynolds number and the effect of different nozzle efflux. At a typical cruise condition $AoA_{eng} = 4.25°$, the pair of isolated engines E2 has a C_{D^*nac} of 52dc which is approximately 22.2% of the clean aircraft total drag. Across the computed range of incidence the lift coefficient ($C_{L\,eng}$) for the baseline engine E1 was relatively small and increased from 0 to 0.008. For the same range of incidence, the $C_{L\,eng}$ for the E2 engine increased from 0 to 0.012. For the effective incidence onto the engine of approximately $4.25°$ at the cruise condition, the lift force is

negligible at approximately 0.004% and 0.006% of the lift force for the clean airframe of the cruise lift of $C_L = 0.5$, for the E1 and E2 engines respectively.

The key differences between the engines are observed in the exhaust region due to the different specific thrusts which result is different Mach number distributions for the jet of the by-pass nozzle (Fig. 8a and b). As a result of the relatively high FNPR of 2.71 for E1 engine, a set of expansion and compression waves arise in the jet which is reflected in the pressure distribution by the negative pressure that occurs between 20% and 60% of the core cowl length ($L_{core\ cowl}$). Nevertheless, the overall force on the exhaust $\theta_{exhaust}$ is beneficial and corresponds to 11.1% of the calculated standard net thrust. For the low specific thrust engine E2, the FNPR of 2.11 results in a different flow topology and a relatively constant distribution of positive pressure coefficient $C_p = +0.3$ that acts on the surface of the core cowl. This provides a beneficial forward oriented force ($\theta_{exhaust}$) which corresponds to approximately 18% of $F_{N\ ref}$. For the larger engine with the lower specific thrust and concomitant reduced FNPR, these beneficial changes in $\theta_{exhaust}$ on the core cowl make it relatively easier to achieve the same values of modified thrust (F_N^*) to compensate for the increase in modified nacelle drag (D_{nac}^*)

The nacelles for both engines were designed based on typical design guidelines and the computations indicate a plausible design of the nacelle with a peak Mach number of 1.06 and 1.08 at the nacelle forebody at zero incidence, for the E1 and E2 engines respectively. The intake and nacelle performance is considered acceptable for this study with no intake separations, conventional pressure distributions over the nacelle, inlet pressure recovery of 0.998 and a nominal fan face M of 0.54 at $AoA_{eng} = 4.25°$ (Fig. 8a and b).
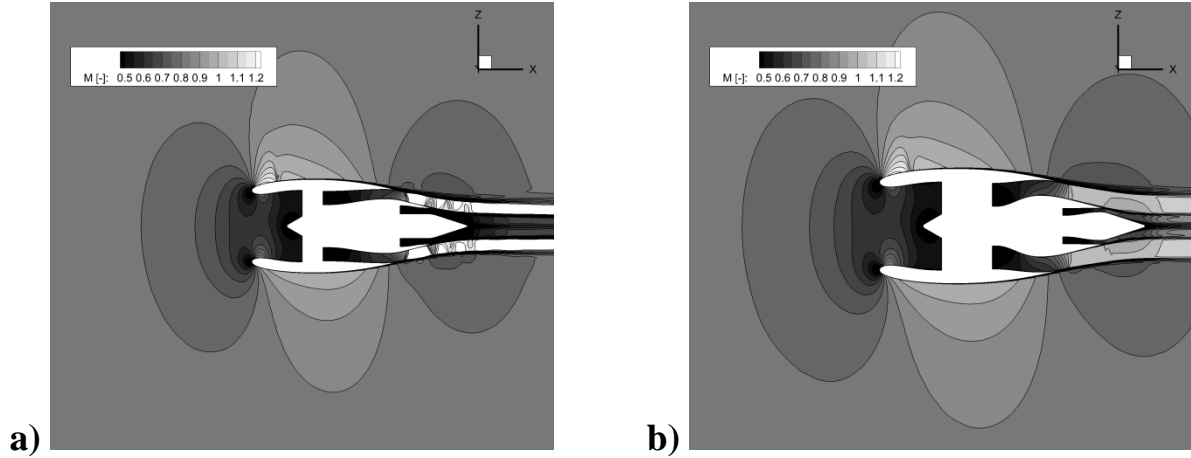
Fig. 8 Mach number contours for a) E1 engine and b) E2 engine at $Re = 45x10^6$, $M = 0.82$, $AoA_{eng} = 4.25°$

C. Wing-installed engines

1. The effect of engine position on the overall installation for the baseline E1 engine

To investigate the impact of the E1 engine position on the aerodynamic effects of engine installation and interference terms a set of evaluations were performed at nine engine (Fig. 2). For each engine position the interference terms are determined from RANS simulations of the combined airframe-engine configurations as well as the clean wing and isolated engine configurations (Equation (7)). Re-trimmed aircraft configurations are considered at cruise condition $M = 0.82$ for an overall vertical force coefficient $C_{z'} = 0.5$ that includes the vertical component of thrust. An assessment of the overall installation effect (F_{inst}) of the baseline E1 engine is considered, as well as, its sensitivity to engine position (Fig. 9). The F_{inst} is decomposed into the drag (D_{nac}^*) and thrust elements ($\theta_{exhaust}$) for the isolated engine as well as the interference terms for the engine (ΔD_{nac}^*; ΔF_N^*) and the airframe ($\Delta D_{A/F}$). The results are referenced to the value of standard net thrust of the baseline engine E1 at cruise condition ($F_{N\,ref}$). For the bare engine, the added $+11\%$ $F_{N\,ref}$ benefit from $\theta_{exhaust}$ is offset by the -14% $F_{N\,ref}$ drag penalty associated with the nacelle (D_{nac}^*) to provide an isolated Net Propulsive Force (NPF) -3.2% penalty relative to the bare engine standard net thrust (F_N).

To evaluate the interference terms due to the installation onto the aircraft, the interference for thrust (ΔF_N^*), modified nacelle drag (ΔD_{nac}^*) and airframe drag ($\Delta D_{A/F}$) are considered in the installation force diagram (Fig. 9). For the different installation positions there are different sensitivities of the interference forces which ultimately affect the final resultant force (F_{inst}). The overall sensitivity of F_{inst} to the engine position is 1.7% $F_{N\,ref}$ depending on the engine location. The decomposition of the overall effect on to the individual interference terms is assessed. The interference on thrust (ΔF_N^*) is predominantly sensitive to the engine axial position and the overlap of the exhaust with the wing (positions C, $\Delta X/L_{nac} = -0.06$; Fig. 2). For these cases there is a penalty where $\Delta F_N^* < 0$ which reduces the obtained engine thrust (F_N^*). For the group of positions A and B ($\Delta X/L_{nac} = -0.45$ and $\Delta X/L_{nac} = -0.26$), the changes in ΔF_N^* are relatively minor with a slight beneficial effect of $\Delta F_N^* < +1\%$. For all installation positions the interference effect on the nacelle (ΔD_{nac}^*) is advantageous with benefits in the order of $+2.6\%$ to $+5.1\% F_{N\,ref}$. These benefits are slightly more pronounced for the group of engines in positions A and B which are further forward of the wing leading edge (Fig. 9). The largest change in ΔD_{nac}^* is $+5.2\% F_{N\,ref}$ which arises for position A2 and partially offsets the -14% associated with the isolated nacelle drag D_{nac}^*. In general, for all engine positions, there is an adverse effect on the airframe with a penalising $\Delta D_{A/F}$ which ranges from -0.3% to $-6.6\% F_{N\,ref}$. The engines in the relatively close axial position (positions C, $\Delta X/L_{nac} = -0.06$) have less of an impact on $\Delta D_{A/F}$ (Fig. 9). However, the engines positioned further forward (positions B, $\Delta X/L_{nac} = -0.26$ and positions A, $\Delta X/L_{nac} = -0.45$) have a more notable impact with $\Delta D_{A/F}$ in the range of -4.7% to $-6.6\% F_{N\,ref}$. This typically offsets the previous benefits in ΔD_{nac}^* for this family of installation positions.

To indicate the sensitivities of the interference effects, a map of the overall interference (F_{interf}) effects was created based on the nine engine positions for the E1 engine (Fig. 10) with use of natural neighbour interpolation [45] based on Delaunay triangulation. Although nine points are relatively few to create detailed contour maps, the visualization was considered helpful to understand the key sensitivity at a preliminary design stage. In the considered range the best position is C3 and other results were presented as relative to this position. Based on the interference map (Fig. 10), a trend along the C3-A1 diagonal is observed. Movement of the engine closer to the wing vertically or upstream axially was detrimental as compared with position C3. The worst position is A2 where it is approximately -1.7% of reference thrust relative to C-3.
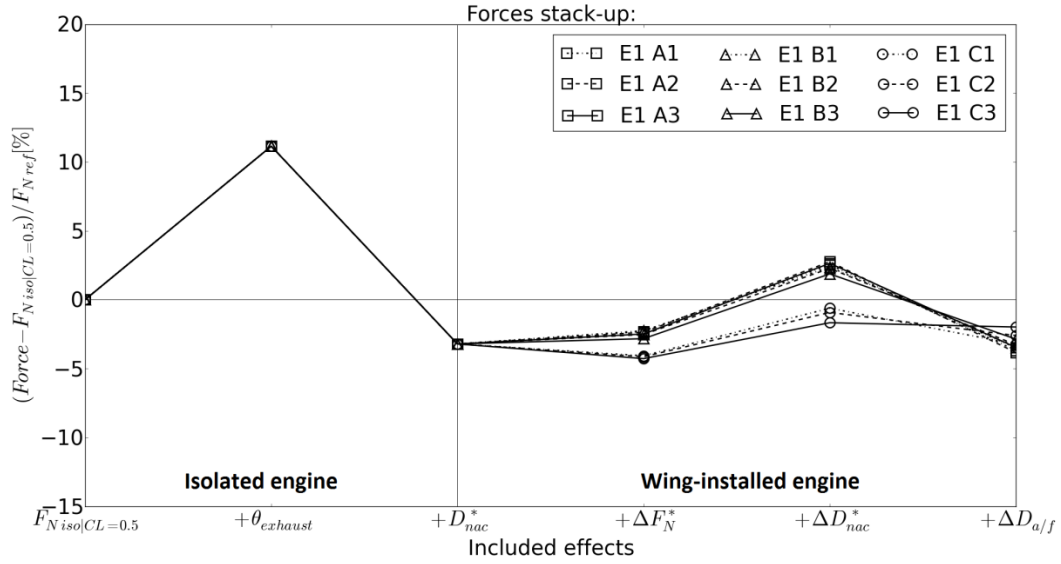
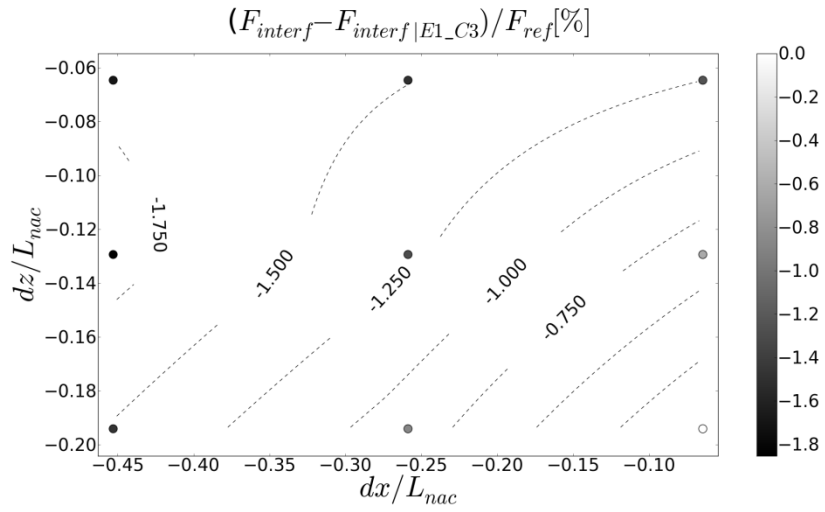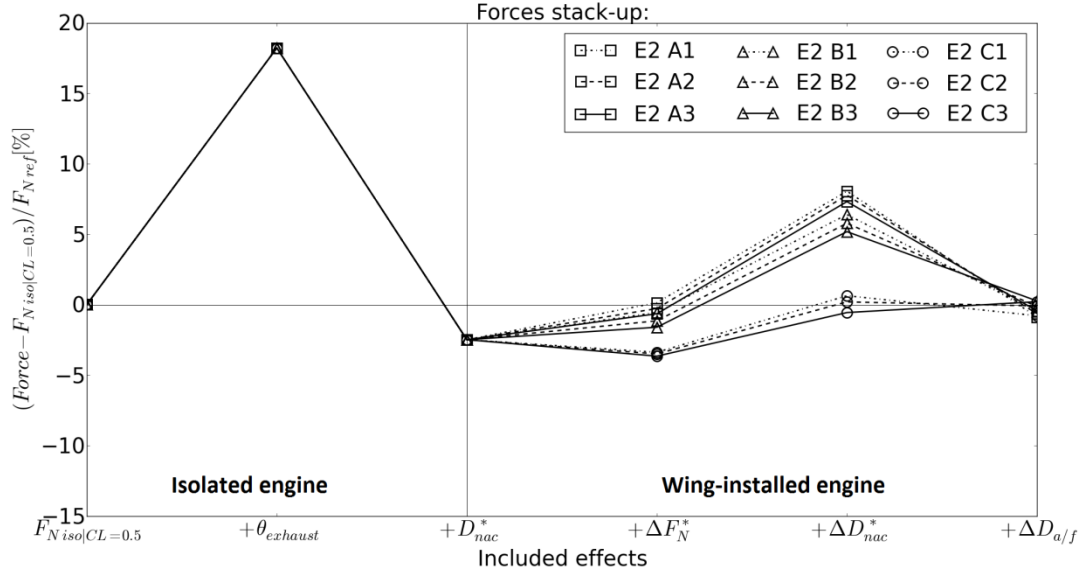**Fig. 9 Overall installation force diagram for E1 engine in a range of under-wing positions.**

Fig. 10 The overall interference (F_{interf}) for baseline engine (E1) for dx and dz engine displacements.

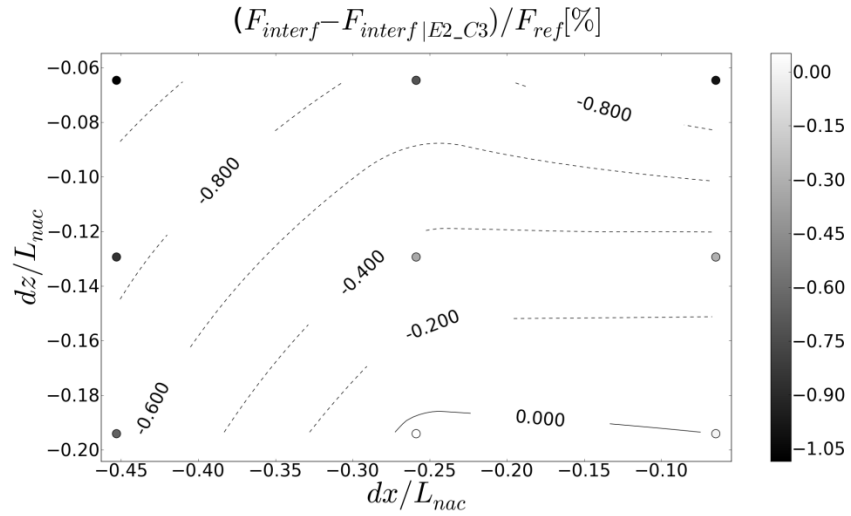*2. The effect of engine position on the overall installation for the E2 engine*

The impact of engine position on the overall installation effect for the larger engine E2 was also considered. The E2 engine was tested for the same range of positions as engine E1 and between the two engine sizes the location of nacelle trailing edge ($\Delta X/L_{nac|E1}$; $\Delta Z/L_{nac|E1}$) was kept constant. Similarly, the installation force diagram (Fig. 11) for the E2 engine was created to decompose the overall installation effect (F_{inst}) in to the drag (D_{nac}^*) and thrust ($\theta_{exhaust}$) terms for isolated engine as well as the interference terms (ΔF_N^*, ΔD_{nac}^*, $\Delta D_{A/F}$). For this larger E2 engine, the effect of the $\theta_{exhaust}$ is $+18\%$ $F_{N\,ref}$ which is offset by $-21\%F_{N\,ref}$ for the D_{nac}^* to give an overall NPF for the isolated engine which is -2.5% lower than the bare engine standard net thrust (Fig. 11). As expected, for aerodynamically similar nacelle designs for E1 and E2, the engine modified drag (D_{nac}^*) approximately scales with the engine fan area. However, as for the $\theta_{exhaust}$, the benefits are approximately $+2\%$ greater than an evaluation based on the geometrical relation between the engines. It is explained by the reduced and more favourable FNPR for E2 engine as compared with E1. Overall, the isolated engine E2 performed $+0.7\%$ better than E1 engine in terms of the isolated net propulsive force.

For the E2 engine, there are some notable differences in the interference terms which depend on the engine position and overall the final installed NPF varies by 1.3% $F_{N\,ref}$ across the full range of positions (Fig. 11). This is less than the range of 1.7% which was calculated for the smaller E1 engine across the same range. For the E2 engine, the effects of the interference reflect some of the aspects observed for the smaller E1 engine. For example (Fig. 11), the group of engines positioned closest to the wing leading edge ($\Delta X/L_{nac|E1} = -0.06$, C1, C2, C3) exhibit a negative effect of the exhaust interference (ΔF_N^*) of approximately -1% $F_{N\,ref}$. The other engines positioned further upstream show a beneficial impact from about $+0.9\%$ to $+2.6\%$ $F_{N\,ref}$. All of the engines show a beneficial impact of the interference on the nacelle across the range of $+3\%$ to $+8\%$ $F_{N\,ref}$ with, in general, the largest benefits observed for the engines furthest upstream of the wing with $\Delta X/L_{nac|E1} = -0.45$ (group A). The effect of interference on the aircraft ($\Delta D_{A/F}$) ranges from slightly positive ($+0.8\%$) for the close coupled position C3 ($\Delta X/L_{nac|E1} = -0.06$, $\Delta Z/L_{nac|E1} = -0.26$) to significantly negative of up to -9% for the other configurations further upstream (groups A and B).

Fig. 11 Overall installation force diagram for engine E2 in different engine positions.

The sensitivity of the overall impact on the resultant force (F_{inst}) depends on the balance of these competing interference elements and is visualized based on the Delaunay triangulation as previously for the range of non-dimensional positions $\Delta X/L_{nac|E1}$ and $\Delta Z/L_{nac|E1}$ (Fig. 12). The spatial sensitivity of all configurations is presented as related to the configuration C3 (Fig. 12). For the larger E2 engine, the best engine locations with the greatest resultant force are B3 and C3. This is further upstream than the best position for the smaller E1 engine which was at C3. The distribution highlights the reduced sensitivity of the resultant force (F_{inst}) due to the installation position for the E2 engine (Fig. 12) as compared with the E1 engine (Fig. 10). The greatest penalty for the E2 engine is observed at the A1 position, which is similar to the highest penalty for E1 at the positions A1 and A2. However, the detrimental effect for the engine at position A1 for E1 engine is approximately 1.5 times greater than for the E2 engine.

Fig. 12 The overall interference (F_{interf}) for the E2 engine for the dx and dz engine displacements.

3. *The effect of engine size on the overall installation effects*

To evaluate the impact of engine size on the installation effects, two size engines are considered over a range of positions. The baseline engine E1 ($D_{FF\ Base}$, Fig. 13a) is compared with the very-high by-pass ratio engine E2 ($1.23 D_{FF\ Base}$, Fig. 13b) and over the range of engine positions considered, the position of the trailing edge point of the nacelle top-line was kept constant between the engines.
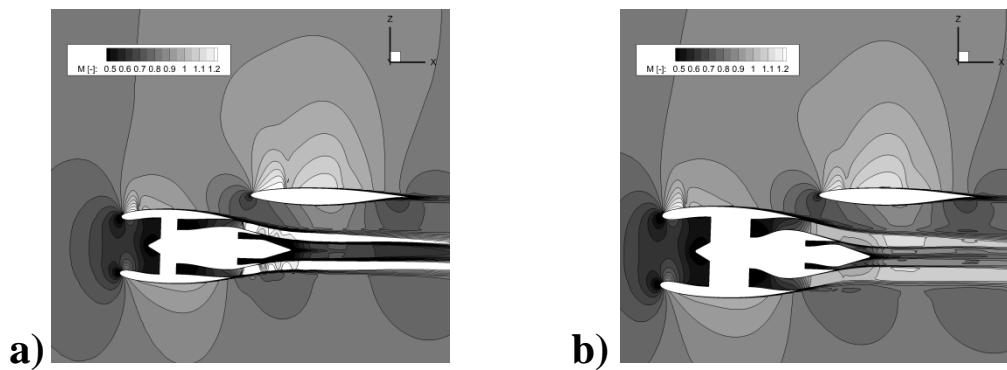

Fig. 13 Contours of Mach number for C3 configurations a) with E1 and b) with E2 engine.

The replacement of the E1 engine with E2 engine resulted in notable changes to the flowfield (Fig. 13) and wing aerodynamics. For example, an initial inspection of the overall Mach number field distribution (Fig. 13) at a typical

cruise incidence of $AoA_{A/C} = 2.5°$, shows a reduction of the peak suction on the upper side of the wing and the

upstream movement of the shock. The changes in the local aerodynamics led to the overall effect in the aerodynamic

forces and the installation of the engine resulted in the increase of total drag $(C_{D\ tot})$ (Fig. 14) which is the sum of

airframe drag $(C_{D\ A/F})$ and the nacelle drag (C_{D^*nac}). At a constant overall vertical force that includes aerodynamic

lift and the vertical component of thrust, the $C_{D\ tot}$ increased by 27 dc for the E1 configuration and by 36 dc for E2

configuration, as compared with the clean wing airframe. The installation penalty in the drag domain is

approximately proportional to the increase of engine size as the drag of the nacelle is the dominant component of the

installation drag. The changes in the aerodynamics also affected the lift force of the aircraft. For the baseline engine

E1 at a typical cruise incidence of $AoA_{A/C} = 2.5°$, the effect of loss of lift as compared with the clean wing

configuration was $\Delta C_{L\ tot} = -0.015$. The loss of lift is predominantly an effect of changes to local wing

aerodynamics, as the engine contribution to the lift force was $C_{L\ nac} = +0.001$ and vertical component of thrust

+0.005 As compared with the baseline engine E1, the E2 engine resulted in a further reduction of lift coefficient of

$\Delta C_{L\ tot} = -0.020$ with a negligible beneficial contribution of the nacelle $C_{L\ nac} = +0.002$ and vertical component

of thrust +0.007.
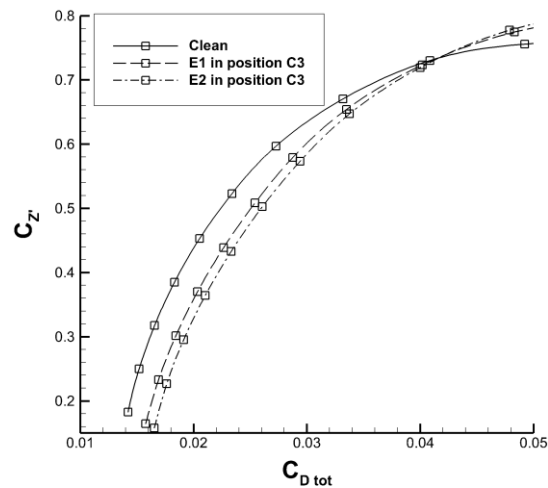
Fig. 14 Overall vertical force ($C_{Z'}$) and drag ($C_{D\ tot}$) polar for CRM with and without engines.

The effect on the aircraft aerodynamic performance is predominantly the result of changes to the pressure

distribution. It has been determined that the changes of the viscous forces due to the increase of engine size are

triggered mainly by the upstream movement of the shock location on the upper side of the wing. The magnitude of

the contribution to overall drag force is broadly two orders of magnitude less significant than the changes to the pressure distributions. The impact of the larger engine as compared with the baseline engine on the pressure distribution is of interest for the wing cross-section closest to the installation at y/(b/2)=0.3 (Fig. 15), where y is the spanwise distance from the aircraft axis and b is the span of the wing. As compared with the clean wing (Fig. 15) the installation of the baseline engine E1 reduced the peak suction at the wing upper side by $\Delta C_p = +0.3$ at x/c=0.05 and caused the movement of the shock from x/c=0.45 to 0.25 with a simultaneous increase of shock strength. Compared with the baseline engine E1 (Fig. 15), the installation of the larger engine E2 caused a further decrease of the peak suction by $\Delta C_p = +0.1$ and a upstream movement of the shock by $\Delta x/c = -0.05$. The pressure distribution on the aft section of the wing beyond $x/c = 0.6$ for both engines is coincident with the pressure distribution of the clean wing airframe. For both engine-airframe configurations E1 and E2 (Fig. 15), the reduction of the suction on the upper side of the wing leads to a reduction of local lift coefficient and as a consequence a local reduction of lift induced drag on the wing. Compared with the clean wing (Fig. 15) the installation of baseline engine E1 also changed the pressure distribution on the lower side of the wing. The increased acceleration $\Delta C_p = -0.25$ occurs towards the wing leading edge $x/c = 0.05$. Beyond x/c=0.1 a beneficial effect of increased pressure is observed with a maximum increase of $\Delta C_p = +0.3$ at approximately x/c=0.4. The pressure distribution for the aft section of the wing ($x/c > 0.7$) of the E1 configuration is the same as the distribution for the clean wing. Compared with the E1 engine (Fig. 15), the installation of larger E2 engine resulted in broadly the same peak acceleration at the wing leading edge and a relatively modest increase of pressure by $\Delta C_p = +0.05$ at x/c=0.1 and at x/c=0.5. The E2 engine has a significantly lower fan nozzle pressure ratio (FNPR) of 2.11 as compared with 2.71 for E1 engine. The increased suction on the lower side of the wing for the E1 configuration is a result of stronger influence on the wing surface from the expansion waves in the jet.

On the inboard side of the engines (y/(b/2)=0.2, Fig. 15a), the presence of the installation causes an increase of peak suction by $\Delta C_p = -0.1$ on the upper side of the wing for both engine configurations and it moves the shock location forward by $\Delta x/c = -0.2$ and $\Delta x/c = -0.25$ for E1 and E2 configurations, respectively. On the lower side of the wing (y/(b/2)=0.2), a significant flow acceleration $\Delta C_p = -0.25$ is observed between x/c=0.05 and x/c=0.2.

The changes to the pressure distribution on the wing affect the spanwise lift distribution. On the inboard side of the engine between y/(b/2)=0.1 and 0.3 (Fig. 15b), the magnitude of the reduction of local lift coefficient is below -0.04

and -0.05 for E1 and E2 configuration, respectively. On the outboard side of the wing (y/(b/2)=0.4, Fig. 15c), the presence of the installation reduced the peak suction on the upper side of the wing by $\Delta C_p = +0.2$ and $\Delta C_p = +0.3$ for E1 and E2 configuration respectively. A two shocklets in the pressure distribution are noted at approximately x/c=0.2 and x/c=0.6 for both engine configurations as compared with a single shock at x/c=0.4 for the clean-wing. The impact of the installation on the lower side of the wing is modest for the outboard side of the wing (y/(b/2)=0.4, Fig. 15c). As a result of pressure distribution, the local loss of lift reduces to less than -0.01 on the outboards side of the engine (y/(b/2)>0.4, Fig. 15c and d) and no difference between the two engine configuration is observed at approximately y/(b/2)=0.6 and further to the tip of the wing.
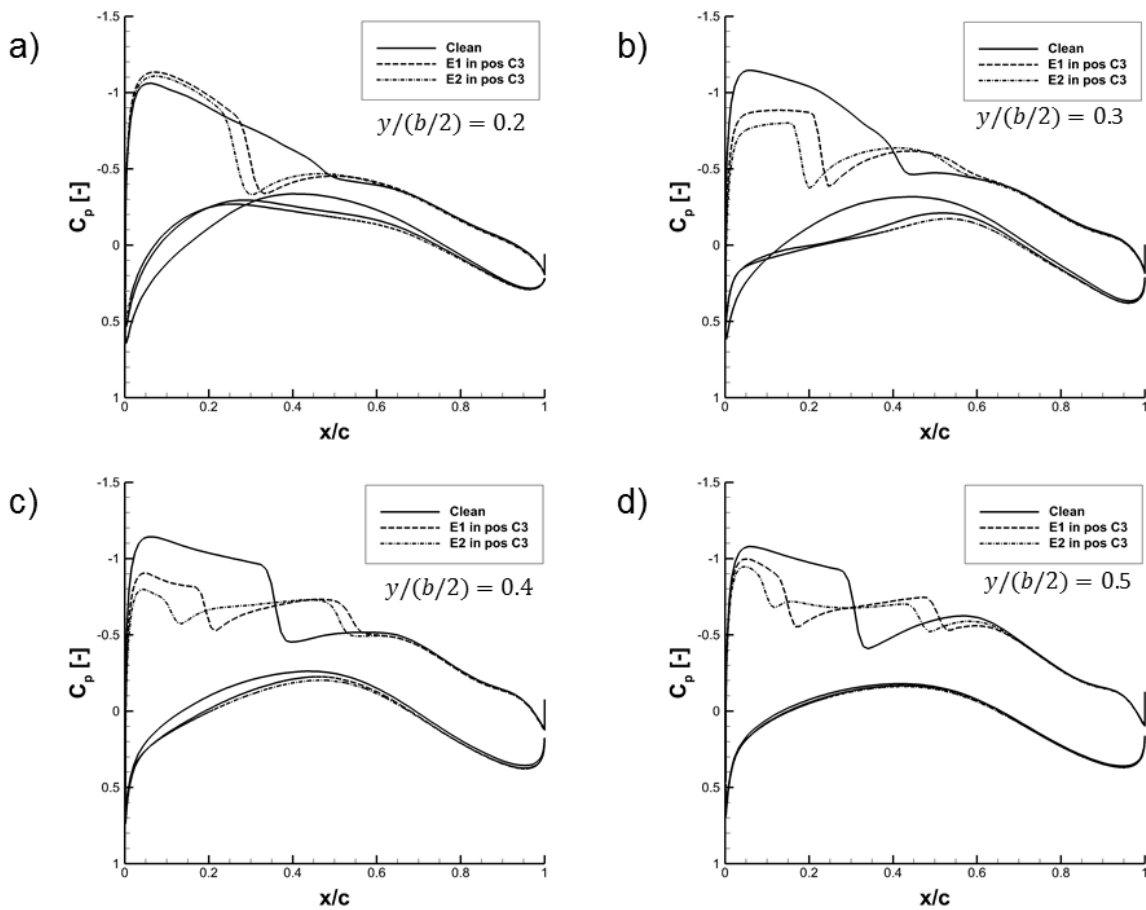

Fig. 15 Pressure distribution for aircraft with and without engines; $Re = 45 \times 10^6$; $M = 0.82$; $AoA_{A/C} = 2.5°$; $y/(b/2)$ from 0.2 to 0.5

To localize the changes in pressure and viscous forces and to highlight the importance of the changes to the overall drag, the difference of local drag force per unit area between the E1 configuration and the idealized 'no-interference'

configuration is calculated (Fig. 16a). As for the upper side of the wing (Fig. 16a), the installation of the E1 engine reduced the local drag due to the movement of the shock location upstream on the inboard side of the installation. The changes to the drag occur predominantly for the root and centre sections of the wing with negligible difference to the wing tip. The wing pressure-field affects the force distributions on the engine. The fan cowl, core cowl and plug surfaces were presented in cylindrical coordinate system (ξ, Θ) (Fig. 17a). A notable beneficial effect on the afterbody of the fan cowl is present due to the forward pressure force exerted by the wing pressure field. Moreover, the shock pattern in the jet was affected by the interaction with the pressure field and the force distribution on the core cowl was changed but no overall beneficial trend is observed. At the surface of the plug, a beneficial pressure force is also exerted due to the pressure-field of the wing. Furthermore, the difference in drag distribution between the E2 configuration compared with the clean-wing and isolated engine was done (Fig. 16b). The installation of E2 engine caused a greater reduction of drag at the root of the wing as compared with the E1 engine. For the engine surfaces, the beneficial pressure force is exerted by the wing pressure-field. Modest interaction of the wing pressure-field with the jet is observed in the forces distribution, due to the relatively low FNPR for the E2 configuration (Fig. 17b) as compared with the E1 engine. A modest beneficial pressure force is exerted by the wing pressure field on the surface of the engine core cowl.
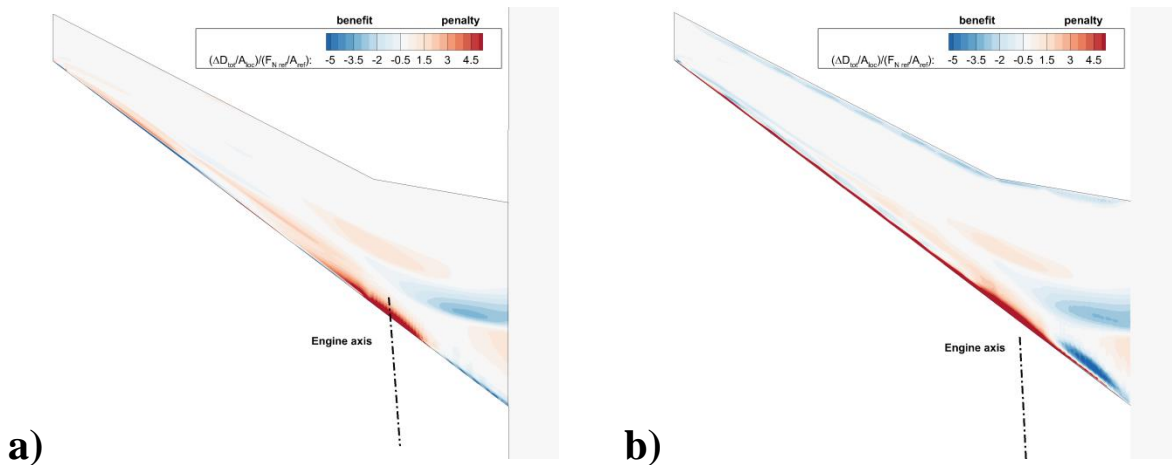
Fig. 16 Distribution of difference drag ($\Delta D_{tot}/A_{loc}$) between a) configuration E1; b) configuration E2 and the clean-wing.
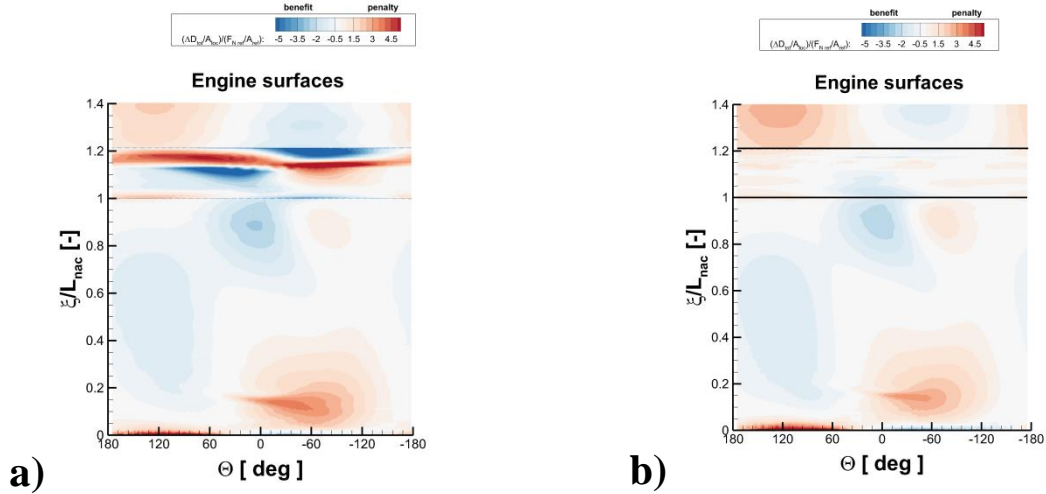
Fig. 17 Distribution of difference drag (ΔD_{tot}) between a) configuration E1; b) configuration E2 and isolated engine.
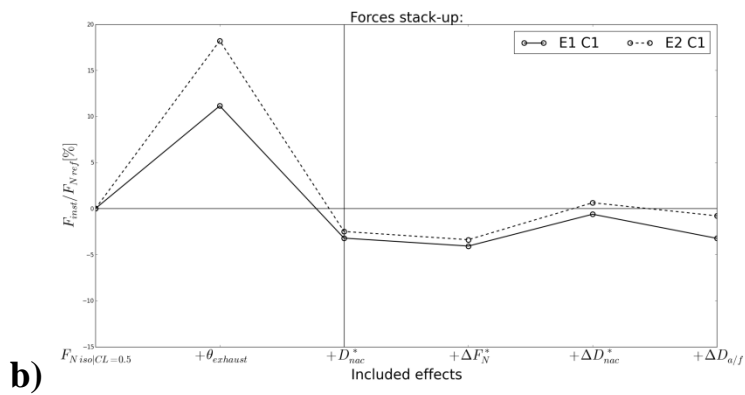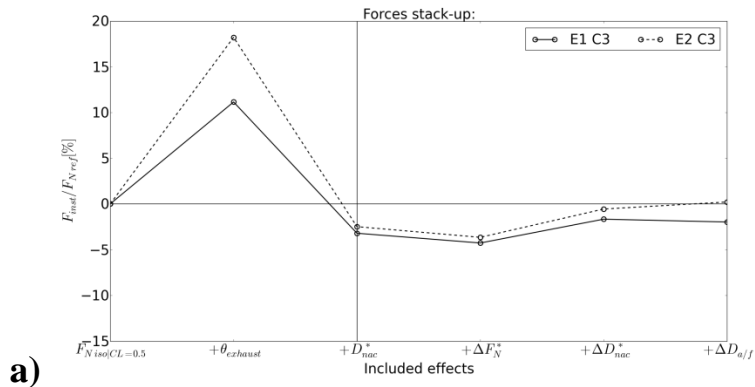
To quantify the overall installation effect, a force diagram (Fig. 18) for the two engines E1 and E2 was developed. The cruise operating point was chosen with the coefficient for the overall vertical force of $C_{z'} = 0.5$ at M=0.82. The installation effects are considered for a re-trimmed aircraft and are referenced to the value of standard net thrust of the baseline engine E1 at cruise condition ($F_{N\,ref}$) (Fig. 18). The isolated net propulsive force (NPF) is deconstructed into beneficial thrust terms (F_N and $\theta_{exhaust}$) and detrimental modified nacelle drag (D_{nac}^*) for both engines. As a result, the difference in isolated NPF between the two engines is determined to be a benefit of $+0.7\ F_{N\,ref}$ for the larger engine E2.

To include the interference terms due to the installation onto the aircraft, the interference for thrust (ΔF_N^*), modified nacelle drag (ΔD_{nac}^*) and airframe drag ($\Delta D_{A/F}$) were considered (Fig. 18 a). Considering the overall interference effect (F_{interf}) in baseline position C3, a benefit of $+1.2\%$ of $F_{N\,ref}$ and $+2.7\%$ of $F_{N\,ref}$ was observed for the engines E1 and E2, respectively. The overall difference in the installation force (F_{inst}) between the two engines is $+2.2\%$ for the larger engine as a result of benefits in isolated NPF and advantageous interference (F_{interf}) as compared with the baseline engine. The benefit for E2 as compared with E1 is explained by an improvement in ΔD_{nac}^* by $+0.4\%\ F_{N\,ref}$ and in $\Delta D_{A/F}$ by $+1\%\ F_{N\,ref}$ for the E2 engine. Meanwhile, a very modest difference

between the engines is observed in ΔF_N^* by $+0.1\%$ $F_{N\,ref}$ in favour of E2 engine. Moreover, the sensitivity of overall interference and the sensitivity of the individual terms is dependent on the engine position. By locating of the engines vertically closer to the wing (position C1, Fig. 18 b), the overall installation force (F_{inst}) increased by $+2.45\%$ $F_{N\,ref}$ for the E2 engine as compared with E1 at corresponding position. The major advantage for the larger engine comes from the improvement in $\Delta D_{A/F}$ by $+1.2\%$ $F_{N\,ref}$, as the improvement in ΔD_{nac}^* is $+0.5\%$ $F_{N\,ref}$ and the effect on ΔF_N^* is neutral as compared with E1. The movement of the engines upstream from the wing affected the interference terms significantly (position A1, Fig. 18 c). A notable benefit in ΔF_N^* of $+1.7\%$ $F_{N\,ref}$ and improvement in ΔD_{nac}^* by $+3.1\%$ $F_{N\,ref}$ are observed for the E2 engine as compared with E1 at a corresponding position. However, the interference on airframe $\Delta D_{A/F}$ became more penalising for the larger engine by -2.7% $F_{N\,ref}$ and it offsets the gains from the thrust and nacelle interferences. As a result, the difference in the overall installation force between E2 and E1 engines at position A1 results in $+2.8\%$ $F_{N\,ref}$ for E2 engine. To assess the spatial sensitivity of the overall installation effect, a map of difference in F_{inst} is considered (Fig. 19). Apart from the benefit for E2 as compared with E1 in terms of isolated NPF ($+0.7\%$ $F_{N\,ref}$), the additional difference in F_{interf} is considered. The difference in overall installation effect between the two configuration is a result of considerably different sensitivities of interference effect (F_{interf}) for each engine. Relative to the E1, the $+2.2\%$ $F_{N\,ref}$ benefit for E2 engine at position C3 increases up to $+3.2\%$ $F_{N\,ref}$ benefit for E2 at position A2. Even though, the position A2 is less favourable for both engines as compared with C3, it is relatively advantageous to locate a larger engine in position A2, if other design constraints require it.

It is useful to compare these results for the impact of engine size with previous experimental studies [2, 3, 4]. These studies using TPS systems for a range of engine sizes indicated that the installation penalty ranged from about 35dc to 42dc for a range of engine sizes from D_{FF}/c_{loc} of 0.42 to 0.51. These experimental studies were also under nominal cruise conditions although the Mach number was notably lower with 0.75 [2]. The current computational studies have been conducted at a nominal cruise condition of M=0.82 and the initial nominal reference condition for the engines is the standard net thrust ($F_{N\,ref}$). To ensure compatibility with the previous experimental work, the current analysis is modified to present installation drag within the same definition [2]. Taking this into account, and keeping in mind that these are the changes in the drag domain only, the current computational results indicate a

typical installation penalty ($C_{D\ inst}$) of 33dc for the E1 engine ($D_{FF}/c_{loc} = 0.36$) and 45dc for the E2 engine ($D_{FF}/c_{loc} = 0.45$). For each of these engines, the $C_{D\ inst}$ varies with position by 5dc and 3dc for the E1 and E2 engines, respectively. Although the current configurations and operating conditions are different, the overall effect is broadly in agreement with these previous experimental studies. However, a different approach was followed for the accounting of the thrust, as compared with the previous studies [2, 3, 4]. Due to the design of the engines for the same standard net thrust (F_N) and explicit presentation of the exhaust forward force ($\theta_{exhaust}$) a benefit in aerodynamic forces for the larger engine (E2) is observed. Overall, as compared with the baseline (E1) engine, the large engine (E2) requires from -2.2% to -3.2% less thrust to compensate for the overall installation penalties over the range of considered positions. The large penalties of the modified drag of the nacelle (D_{nac}^*) increased proportionally to the engine size, however, they were offset by the better interference terms and the beneficial effect on the exhaust term ($+\theta_{exhaust}$) due to the design of the core cowl and plug as well as the favourable lower FNPR.

a)

b)

c)
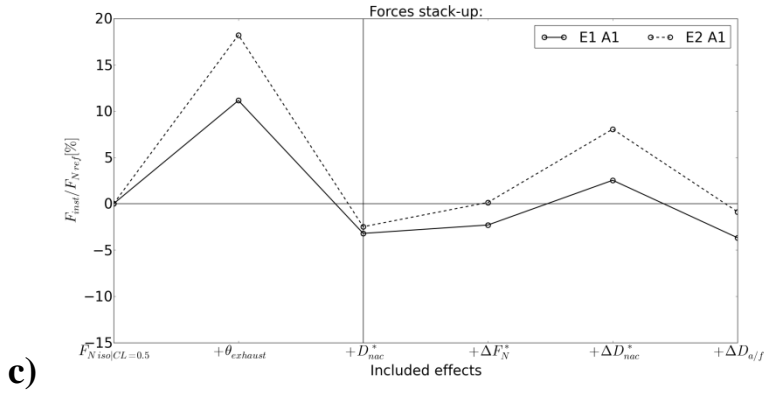
**Fig. 18 Installation force for E1 and E2 in positions a) C3 b) C1 and c) A1.**
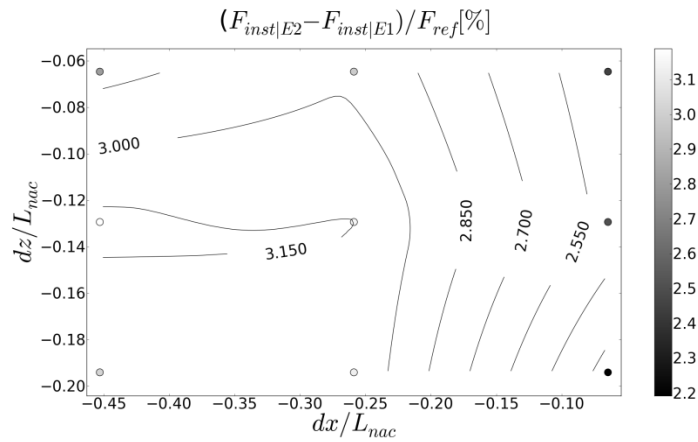
Fig. 19 The difference in overall installation effect ($F_{inst|E2} - F_{inst|E1}$) between E2 and E1 engines.

4. Cruise fuel burn analysis

To quantify the effect of engine position in terms of fuel consumption, a single point calculation at the start of cruise 'SoC' condition was initially considered to compare the engine fuel flow (Fig. 20) based on the thrust requirement for the balanced aircraft. For the baseline engine E1, the spatial sensitivity of aerodynamic forces to different engine position results in a greater thrust requirement for some of the engine positions as compared with the baseline position C3. As a result, the fuel consumption ($\dot{m}_{fuel}$) of the engine rises by approximately +1.6% in the worst position A2 as compared with the best installation position C3.

To compare the fuel consumption between the two engines the cycle performance at the 'SoC' design point was analysed. The benefits in $\dot{m}_{fuel}$ for E2 engine are about -5.8% based on the cycle analysis. The single point calculation for a balanced aircraft at 'SoC' with use of the computed aerodynamic installation effects and the weight penalty for the larger engine resulted in benefits in $\dot{m}_{fuel}$ ranging from -5.6% to -6.6% for E2 as compared with E1 at a corresponding position. The increase of aircraft weight for E2 configurations resulted in a greater lift requirement, and as a consequence greater drag and thrust requirement for the engine. Overall the detrimental effect of weight was in order of +2% increase in $\dot{m}_{fuel}$ that partially offset the benefits from the cycle improvements and aerodynamics. As a result a spatial sensitivity map for the fuel consumption at start of cruise condition was created for the E2 as compared with E1 at corresponding position and referenced to the $\dot{m}_{fuel}$ of E1 at C3 (Fig. 21). The thermodynamic cycle improvements, aerodynamic differences and weight penalty were included (Fig. 21). The -5.6% benefit in $\dot{m}_{fuel}$ for E2 engine as compared with E1 is observed at position C3. Due to different spatial sensitivities for the two engines, the benefit for the large engine E2 increases to a -6.6% reduction in fuel flow rate at position A2.
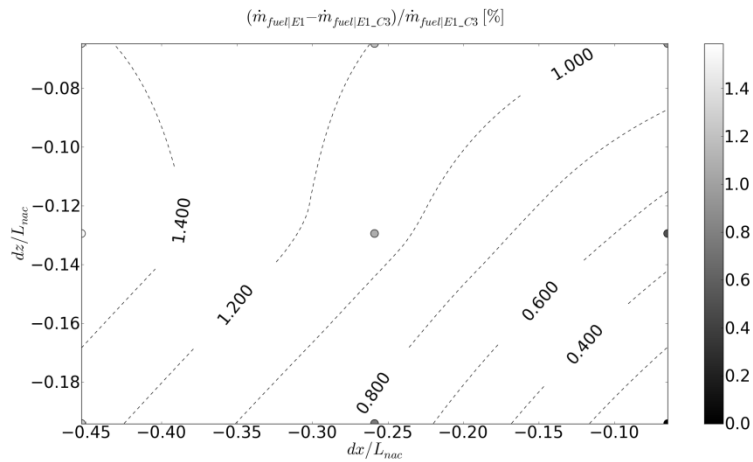
Fig. 20 Sensitivity map of the fuel consumption ($\dot{m}_{fuel}$) for the E1 as compared with E1_C3.

$(\dot{m}_{fuel|E1} - \dot{m}_{fuel|E1\_C3})/\dot{m}_{fuel|E1\_C3}$ [%]
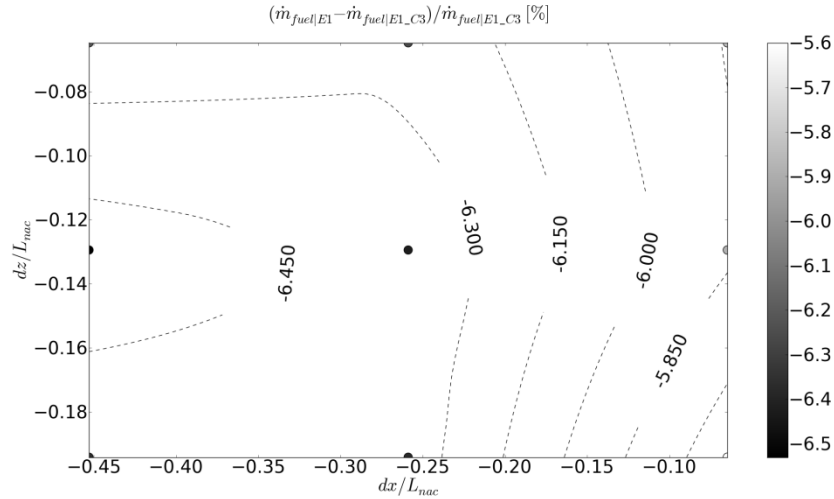
Fig. 21 Sensitivity map of the fuel consumption ($\dot{m}_{fuel}$) for the E2 engine as compared with E1_C3.

To compute the integrated fuel consumption over the entire cruise phase, the throttle dependent aerodynamic effects were considered. A range of engine power settings for E1 and E2 engines in configuration C3 was computed (Table 1), to cover the cruise phase from the start of cruise ('SoC') through end of cruise ('EoC'), as well as to give an indication about the effects at start of descent ('SoDe').

Furthermore, to determine the performance of the engine over the entire cruise phase of flight, the relation between the overall installation force (F_{inst}) and the engine power setting and lift coefficient is considered. Based on the computations for engine E1 in the baseline position C3, a sensitivity map of the overall installation force (F_{inst}) as a percentage of reference thrust ($F_{N\,ref}$) was created (Fig. 22a) to aid the cruise fuel burn analysis. The map covers the range of lift coefficient and range of engine power settings represented by the intake massflow capture ratio (MFCR). For the baseline engine E1, the installation penalty (F_{inst}) increases for aircraft off-design conditions away from $C_{z'} = 0.5$ and $MFCR = 0.75$. The dominant trend is the increase of the installation penalty with reducing MFCR as a result of spillage. The secondary effect observed is the jet interaction with the flow acceleration over the lower side of the wing at MFCR=0.75 and low lift coefficient ($C_{z'} = 0.2$). At $C_{z'} = 0.2$, the reduction of power setting initially alleviates the jet interaction for the MFCR=0.7, however, further reduction of power setting is dominated by the increasing spillage drag. Overall, over the entire range of conditions considered, the sensitivity to engine power setting and aircraft lift coefficient is in order of 3% of $F_{N\,ref}$. Based on the computed relation between

the overall installation force (F_{inst}) and the engine power setting, the integrated cruise fuel burn calculation was considered with the weight penalty for large engine included. For the E1 configuration the 'SoC' condition was evaluated to be at $C_{z'} = 0.47$ and MFCR=0.75 for a fully balanced aircraft at M=0.82 at an altitude of 35000ft. The step calculation method for cruise phase was applied and the 10000 km range was divided in 40 steps. As a result, the end of cruise 'EoC' point was established for the E1 configuration at $C_{z'} = 0.34$ and MFCR=0.7. The integrated fuel burn for the cruise phase was evaluated. A similar off-design performance map was created for the large engine E2 (Fig. 22b). The large engine exhibits a more monotonic behaviour with regards to power setting and lift coefficient as compared with E1 engine. The design of the engine for the low specific thrust resulted in more favourable nozzle pressure ratios and the jet interference effects at the high power setting and low lift coefficients ($C_{z'} = 0.2$) were mitigated.

a)

b)
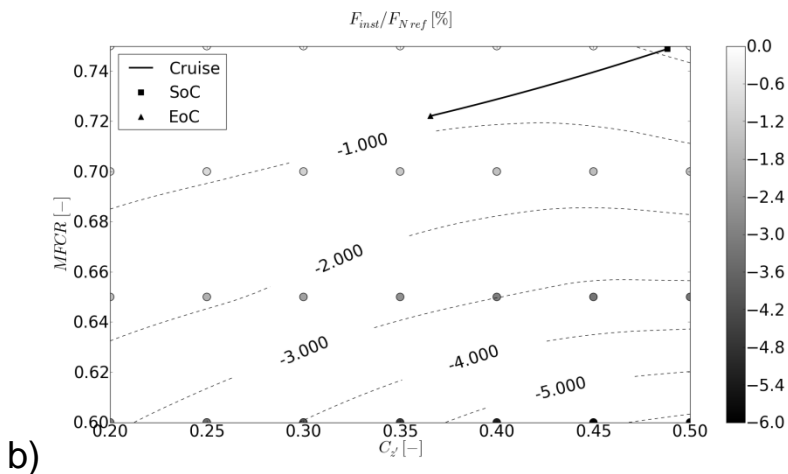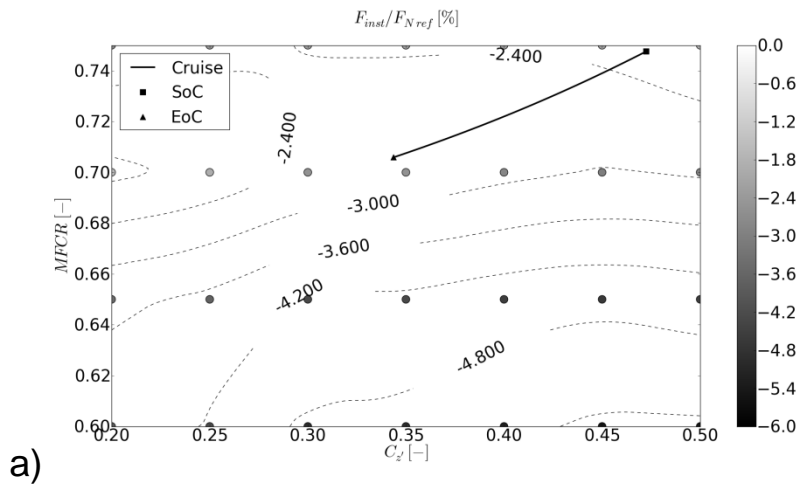
Fig. 22 $F_{inst}/F_{N\,ref}$ for a) E1 and b) E2 over the range of $C_{z'}$ and MFCR

The effect of the engine power setting on the overall installation penalty for the E2 engine is approximately twice as sensitive as the effect of power setting for the E1 engine and it is in order of 5.5% of $F_{N\,ref}$. Based on off-design map for the overall installation effect (F_{inst}) as a function of the engine power setting and aircraft lift coefficient, the integrated cruise fuel burn calculation was considered. For the E2 configuration the 'SoC' condition was evaluated to be at $C_{z'} = 0.49$ and MFCR=0.75 for a fully balanced aircraft. The greater value of the $C_{z'}$ is the result of the increased weight of the aircraft for the E2 configuration as compared with the E1 configuration. The step calculation method for cruise phase was applied for the same mission at M=0.82 over a range of 10000 km. As a result, the end of cruise 'EoC' point was established for the E1 configuration at $C_{z'} = 0.36$ and MFCR=0.72. The integrated fuel burn for the cruise phase was evaluated and as compared with the E1 engine the E2 engine consumed -4.8% less fuel over the same mission. As a consequence, the estimated benefits from the thermodynamic cycle analysis in the order of -5.8% reduced to -4.8% fuel burn reduction in favour of the large E2 engine taking into account the effects of throttle dependent aerodynamic effects, installation terms and the engine weight penalty that were considered over a long-haul mission.

IV.   Conclusion

The effect of engine installation for a typical 300 seater at a cruise condition of M=0.82 and altitude 35000 ft was considered. The sensitivity of the overall installation effect to engine size, position and power setting was evaluated. Depending on the position, the sensitivity of the aerodynamic installation effect ranged within 1.7% and 1.3% of reference thrust for the baseline engine and the larger engine, respectively. The fuel burn during the cruise phase was compared for both engines based on the computed engine-aircraft aerodynamics. Based on the cycle performance, the reduction in fuel burn due to the high by-pass ratio cycle was approximately −5.8%. Moreover, the aerodynamic benefit for the large engine was observed due to favourable aerodynamic interference for the low specific thrust engine. However, the aerodynamic benefits were offset by a detrimental effect of engine weight. For one typical installation position, the single point calculation at the start of cruise indicated the fuel reduction of -5.6% for the larger engine as compared with the baseline engine. Finally, the complete cruise phase was considered with an evaluation of the throttle dependent interference effects. Compared with the baseline engine, the larger

configuration with the -34% lower specific thrust had a nominal cycle benefit of -5.8% which reduced to -4.8%

when the effects of engine weight, installation and throttle dependent interference were included.

Acknowledgments

The authors would like to thank J. C. Vassberg for making available the geometry of the Common Research Model

including the through flow nacelles.

References

1. Daly M, Ed. *Jane's Aero-Engines*, 28th ed., IHS Global Ltd, Surrey, 2010,
2. Hoheisel, H., "Aerodynamic aspects of engine-aircraft integration of transport aircraft",*Aerospace Science and Technology*,Vol. 1, No 7, 1997, pp. 475-487.
3. Brodersen, O. "Computation of Engine-Airframe Installation Drag" *MEGAFLOW - Numerical Flow Simulation for Aircraft Design*, edited by Kroll, N., Fassbender, J.,Vol. 89, Springer, Berlin, 2005. pp. 151-161.
4. Rossow, C-C., Nashville, T. N., "Investigations of Propulsion Integration Interference Effects on a Transport Aircraft Configuration",*AIAA/SAE/ASME/ASEE 28th Joint Propulsion Conference and Exhibit*.,6-8 July 1992. Vols. AIAA 92-3097.
5. Geyr, H. Frhr. Von, Rossow, C. C., "*A correct thrust detemination method for turbine powered simulatiors in wind tunnel testing*",41st AIAA/ASME/SAE/ASEE Joint Propulsion Conference & Exhibit,2005, pp. 1-12. AIAA Paper No. 2005-3707
6. Kroll, N., Rossow, C.C., Schwamborn, D., 'Megaflow - A Numerical Flow Simulation Tool For Transport Aircraft Design' , In: *Congress of International Council of Aeronautical Sciences*, 2002, ICAS-2002-1105.
7. Jung, U., Breitsamter, C., 'Experimental Aerodynamic Investigations on Commercial Aircraft High Lift Characteristics by Large Engine Nacelles', Institute of Aerodynamics, Technische Universitat Munchen, 85748 Garching, Germany.
8. Devine, R., Cooper, R.K., Gault, R., 'Comparison of Conventional and Compression Pylon Designs for an Underwing Nacelle', *Journal of Aircraft*, Vol 46. No.1 January-February 2009.
9. Gisin, Y. M., Marshall, D. D., 'Wing-Nacelle Assembly Multidisciplinary Performance Optimization' , In: *45th AIAA Aerospace Sciences Meeting and Exhibit*, 8-11 January 2007, Reno, Nevada, AIAA 2007-1463.
10. Oliveira, G.L., Trapp, L.G., Puppin-Macedo, A., "Integration Methodology for Regional Jet Aircraft with Underwing Engines", *41st Aerospace Sciences Meeting and Exhibit*, 6-9 January, Reno, Nevada, United States, AIAA Paper No. 2003-934
11. Frink N. T., 2nd AIAA CFD Drag Prediction Workshop. [Online] AIAA, June 21-22, 2003. [Cited: 26.04.2016] http://aiaa-dpw.larc.nasa.gov/Workshop2/workshop2.html
12. Vassberg, J. C., et al. " Development of a Common Research Model for Applied CFD Validation Studies", AIAA. 2008. AIAA Paper No. 2008-6919.
13. Rivers, M. B., Dittberner, A., "Experimental investigations of the NASA Common Research Model in the NASA Langley National Transonic Facility and NASA Ames 11-Ft transonic wind tunnel (invited)", *49th AIAA aerospace sciences meeting including the new horizons forum and aerospace exposition*, Orlando, Florida, US 2010, AIAA Paper No. 2011-1126.
14. Rivers, M. B., "Experimental investigation of the NASA Common Research Model (Invited)", *28th AIAA Applied Aerodynamics Conference*, Chicago, Illinios, US, 2010, AIAA.2010-4218
15. Morrison, J. H., 6th AIAA CFD Drag Prediction Workshop. [Online] AIAA, August 3, 2016. [Cited: 08.02.2016] https://aiaa-dpw.larc.nasa.gov/
16. Advisory Group for Aerospace Research and Development (AGARD), "Special course on Subsonic/Transonic Aerodynamic Interference for Aircraft", AGARD Report No. 712, 1983. Tech. rep. AGARD- R-712
17. Stańkowski, T.P., MacManus, D.G., "Aerodynamics of aero-engine installation", Proc IMechE Part G: Journal of Aerospace Engineering 2016, Vol. 230(14) pp. 2673–2692
18. Mikkelsen, K. L., Myren, D. J., Dahl D. G. and Christiansen, M. D, "Initial Subscale Performance Measurements of the AIAA Dual Separate Flow Reference (DSFR) Nozzle", 51st AIAA/SAE/ASEE Joint Propulsion Conference, Orlando, FL, July 2015, AIAA Paper No. 2015-3883
19. Berry, D.L., "The Boeing 777 Engine/Aircraft Integration Aerodynamics Design Process", in Proceedings of the 19th Congress of the International Council of Aerospace Sciences, 1994, ICAS-94-6.4.4.

20. Palmer, J., "The TURBOMATCH scheme for aero/industrial gas turbine engine design point/offdesign performance calculation" School of Mechanical Engineering, 1983, Cranfield University.
21. Heidebrecht, A., Stańkowski, T., MacManus, D., 'Parameteric geometry and CFD process for turbofan nacelles', In: Proceedings of ASME 2016 Turbo Expo: Turbomachinery Technical Conference and Exposition, June 13-17 2016, Seoul, South Korea, GT2016-57784.
22. Christie, R., Heidebrecht, A., MacManus, D., 'An automated approach to nacelle parameterisation using intuitive class shape transformation curves', In: Proceedings of ASME 2016 Turbo Expo: Turbomachinery Technical Conference and Exposition, June 13-17 2016, Seoul, South Korea, GT2016-57849.
23. Goulos, I., Stańkowski, T., Otter, J., MacManus, D., "Aerodynamic Design of Separate-Jet Exhausts for Future Civil Aero-Engines—Part I: Parametric Geometry Definition and Computational Fluid Dynamic Approach", Journal of Engineering for Gas Turbines and Power, August 2016, Vol. 138 No.081201-1
24. Goulos, I., Otter, J., Stańkowski, T., MacManus, D., "Aerodynamic Design of Separate-Jet Exhausts for Future Civil Aero-Engines—Part II: Design Space Exploration Surrogate Modelling, and Optimization", Journal of Engineering for Gas Turbines and Power, August 2016, Vol. 138 No. 081202-1
25. Kulfan, B., Bussoletti, J., "Fundamental" Parameteric Geometry Representations for Aircraft Component Shapes" In: *11th AIAA/ISSMO Multidisciplinary Analysis Optimization Conference*, American Institute of Aeronautics and Astronautics, 2006.
26. Ceze, M., Hayashi, M., Volpe, E., "A Study of the CST Parameterization Characteristics" In: *27th AIAA Aplied Aerodynamics Conference*, American Institute of Aeronautics and Astronautics, 2009.
27. Frink N. T., 4th AIAA CFD Drag Prediction Workshop. [Online] AIAA, June 20, 2009. [Cited: 10.04.2015.] http://aaac.larc.nasa.gov/tsab/cfdlarc/aiaa-dpw/Workshop4/workshop4.html.
28. Tinoco, E. N., Levy, D., Brodersen, O., "DPW-IV Summary of Participants Data", *AIAA 4th CFD Drag Prediction Workshop*, San Antonio, Texas, 2009.
29. Menter, F. R., "Two-equation eddy-viscosity turbulence models for engineering applications", AIAA Journal, Vol. 32, No. 8, 1994, , pp. 1598-1605.
30. Domel N. D, "Perspectives on Propulsion CFD for Nozzle Applications Relevant to the AIAA Propulsion Aerodynamics Workshop", 51st AIAA/SAE/ASEE Joint Propulsion Conference, Joint Propulsion Conference, Orlando, FL, July 2015, AIAA Paper No. 2015-3778
31. Laue, J., 'Nozzle Performance Investigation And Validation For Installed And Isolated Engines', MSc Thesis, School of Aerospace, Transport and Manufacturing, Cranfield University, 2015.
32. Roache, P.J., "Perspective: a method for uniform reporting of grid refinement studies", *Journal of Fluids Engineering*, Vol. 116, No. 3, 1994, , pp. 405-413.
33. Christie, R., Ramirez, S. and MacManus, D. G., "Aero-engine installation modelling and the impact on overall flight performance", In: *Advanced Aero Concepts, Design and Operations Conference*, 27 June 2014, Bristol, United Kingdom.
34. Stańkowski, T.P., MacManus, D.G., "Engine installation module development for an aircraft mission analysis framework", In: *Advanced Aero Concepts, Design and Operations Conference*, 27 June 2014, Bristol, United Kingdom.
35. Voulgaris, I., Civil Aircraft Nacelle and Afterbody Aerodynamics, Master's thesis, Cranfield University, Bedfordshire, UK, MK430AL, August 2014.
36. ESDU, "Introduction to the Measurement of Thrust in Flight (Air Breathing Ducted Flow Engines)", ESDU. 1981. Tech. rep. ESDU-69006
37. Ministry-Industry Drag Analysis Panel (MIDAP) Study Group, "Guide to in-flight thrust measurement of turbojets and fan engines", AGARDograph No. 237 AGARD. 1979.
38. EUROCONTROL, Base of aircraft data (BADA), 2014. [Online]. Available: http://www.eurocontrol.int/services/bada. [Accessed: 19.04.2016]
39. Greitzer, E.M., Bonnefoy, P.A., de la Rosa Blanco, E., Dorbian, C.S., Drela, M., "N+3 Aicraft Concept Designs and Trade Studies, Final Report Volume 2: Appendices – Design Methodologies for Aerodynamics, Structures, Weight, and Thermodynamic Cycles", Appendix H., NASA/CR-2010-216794/VOL2.
40. Jenkinson, L.R., Simpkin, P., Rhodes, D., "Civil Jet Aircraft Design", Arnold publishers, London 1999.
41. Giannakakis, P., Sethi, V., Jackson, A.J.B., Pilidis, P., 'Evaluation of aero gas turbine preliminary weight estimation methods', The Aeronautical Journal, Vol. 118, No. 1204, pp. 625-641, June 2014.
42. Bradley, A., 'An aero-engine vision of 2020', In: Council of European Aerospace Societies, November 2004, Budapest.
43. Taylor, J.R., 'An introduction to error analysis: the study of uncertainties in physical measurements', University Science Books, Sausalito, California, United States, 1982.
44. Laskaridis, P., Pilidis, P., "An integrated Engine-Aircraft Performance Platform for Assessing New Technologies in Aeronautics", In: International Society for Air-Breathing Engines Conference 2005, ISABE-2005-1165.
45. Sibson, R. (1981). "A brief description of natural neighbor interpolation (Chapter 2)". In V. Barnett. Interpreting Multivariate Data. Chichester: John Wiley. pp. 21–36.